Research Square

Preprints are preliminary reports that have not undergone peer review.
They should not be considered conclusive, used to inform clinical practice,
or referenced by the media as validated information.

NaCl-Assisted Synthesis of Co/CoS2 Heterostructures Encapsulated within N, S Co-doped Carbon Nanotubes as Electrocatalysts for Anion Exchange Membrane Fuel Cells and Rechargeable Liquid-State/flexible Zn-air Batteries

Hyeongseok Seo
Inha University
Hoyeon Kang
Inha University
Sejin Kim
Inha University
Sang Eun Shim
Inha University
Sung-Hyeon Baeck
shbaeck@inha.ac.kr
Inha University

Research Article

Keywords: Zn-air battery, Bifunctional electrocatalyst, Mott-Schottky heterojunction, Heteroatom doping, Oxygen electrocatalysis

Posted Date: September 2nd, 2026

DOI: https://doi.org/10.21203/rs.3.rs-10748997/v1

License: This work is licensed under a Creative Commons Attribution 4.0 International License.
Read Full License

Additional Declarations: No competing interests reported.

NaCl-Assisted Synthesis of Co/CoS_2 Heterostructures Encapsulated within N, S Co-doped Carbon Nanotubes as Electrocatalysts for Anion Exchange Membrane Fuel Cells and Rechargeable Liquid-State/flexible Zn-air Batteries

*Hyeongseok Seo, Hoyeon Kang, Sejin Kim, Sang Eun Shim, and Sung-Hyeon Baeck**

Department of Chemistry and Chemical Engineering, Education and Research Center for Smart Energy Materials and Process, Inha University, Incheon 22212, Republic of Korea

**Corresponding author*

E-mail address: shbaeck@inha.ac.kr

Abstract

The development of durable and cost-effective non-precious metal electrocatalysts for both the oxygen evolution reaction (OER) and oxygen reduction reaction (ORR) is crucial for the practical application of rechargeable Zn-air batteries (ZABs). Herein, we report a highly efficient and electrochemically stable bifunctional electrocatalyst consisting of N, S dual-doped carbon nanotubes (NSCNTs) grown on a porous dodecahedral carbon framework, which encapsulates the Co/CoS_2 heterostructures. The porous architecture, engineered via NaCl-assisted templating combined with Zn evaporation, provides abundant access to active sites and promotes electrolyte penetration and mass transport. Meanwhile, the in-situ grown NSCNTs construct a three-dimensional conductive network that facilitates electron transport and stabilizes the embedded Co-based nanoparticles against aggregation. Furthermore, the N,S dual-heteroatom doping and Co/CoS_2 heterointerface engineering introduce structural defects

and modulating the surface electronic configuration of the catalyst, thereby optimizing the adsorption energetics of reaction intermediates. Benefiting from these integrated structural and electronic advantages, the Co/CoS_2/NSCNT electrocatalyst delivers competitive bifunctional activity, exhibiting an overpotential of 334 mV at 10 mA cm^{-2} for OER and a half-wave potential of 0.874 V for ORR. This enhanced ORR activity leads to the high-power density of 199.15 mW cm^{-2}, when Co/CoS_2/NSCNT is assembled into the anion-exchange membrane fuel cell (AEMFC) cathode. When applied to liquid-state and flexible ZABs, the devices achieve peak power densities of 163.57 mW cm^{-2} and 95.19 mW cm^{-2}, respectively, surpassing those of benchmark Pt/C- and RuO_2-based ZABs. Moreover, both devices demonstrate robust cycling stability over 100 and 25 hours, respectively. These results underscore the effectiveness of synergistically integrating hierarchical porosity, conductive carbon networks, and heterointerface engineering in designing efficient and stable bifunctional electrocatalysts for next-generation flexible and wearable energy devices.

Keywords: *Zn-air battery, Bifunctional electrocatalyst, Mott-Schottky heterojunction, Heteroatom doping, Oxygen electrocatalysis*

1. Introduction

The accelerating depletion of fossil fuels, coupled with growing environmental challenges, has intensified global demand for efficient and sustainable energy conversion and storage systems [1]. Among the various candidates, anion-exchange membrane fuel cells (AEMFCs) and rechargeable zinc-air batteries (ZABs) have emerged as highly attractive energy storage technologies owing to their exceptional theoretical energy densities, cost-effectiveness, inherent safety, and environmentally benign characteristics [2, 3]. However, the kinetics of the

oxygen reduction reaction (ORR) and the oxygen evolution reaction (OER) are inherently sluggish and remain as critical bottlenecks that severely limit the practical performance of AEMFCs and ZABs [4]. Especially, ORR activity for the cathode is a crucial factor that influences the efficiency of the AEMFC [5]. Both reactions involve complex multi-step pathways with oxygen-based intermediates (OH*, O*, OOH*), resulting in large overpotentials and poor cycling efficiency [6]. To mitigate these limitations, precious-metal-based catalysts including Pt/C and RuO_2 have been widely adopted as benchmark materials. However, their prohibitive cost, insufficient durability, and lack of bifunctionality impose considerable barriers to large-scale commercialization [7]. Accordingly, developing the cost-effective, durable, and bifunctional non-precious metal electrocatalysts capable of driving both ORR and OER with high efficiency is essential for advancing the practical deployment of anion-exchange membrane fuel cells and ZABs [8].

Recently, transition metal sulfide electrocatalysts derived from Earth-abundant elements have emerged as promising bifunctional catalysts for ORR and OER, due to their tunable redox states, low cost, and excellent electrochemical activity. Compared to other chalcogenides, transition metal sulfides demonstrate relatively outstanding electrical conductivity, primarily owing to the S 2p orbitals, which promote charge delocalization and narrow the band gap [9]. However, their intrinsic semiconducting character still limits charge transfer efficiency, necessitating further structural and electronic optimization to achieve outstanding electrocatalytic performance. One effective strategy is the construction of heterojunctions between compositionally distinct components, which induces electron density redistribution at the interface and significantly improves charge transfer kinetics [10]. In particular, the intimate contact between a metallic phase and an n-type semiconductor facilitates directional electron transfer across the heterointerface, forming a Mott-Schottky junction with a built-in electric field [11, 12]. Subsequently, the created Mott-Schottky junction promoted the adjustment of

ad/desorption energies of reaction intermediates and electron transport, thereby enhancing the electrocatalytic performance for ORR and OER [13]. Representative examples include CoFe-LDH/Ni_3S_2 heterointerfaces reported by Lang and colleagues, which exhibited excellent OER activity in alkaline solution [14] and nitrogen-doped carbon-coated Cu/Fe_2N demonstrated by Chen et al., which delivered exceptional ORR performance in 0.1 M KOH with a half-wave potential of 0.83 V vs. RHE and a Tafel slope of 66.73 mV dec^{-1} [15]. Among transition metal sulfides, CoS_2 is especially attractive owing to its metallic-like conductivity, favorable d-band electronic structure, and strong affinity toward oxygen intermediates. The deliberate coupling of metallic Co with CoS_2 to form a Mott-Schottky heterojunction is expected to synergistically optimize intermediate adsorption energetics while maintaining rapid electron transfer, a combination rarely achieved in a single non-precious metal catalyst architecture. Despite these advances, simultaneously achieving high bifunctional activity with the long-term cycling stability for a single catalyst system remains a formidable challenge, motivating the rational development of advanced hetero-structured electrocatalysts for practical ZAB systems.

Carbon nanotubes (CNTs) offer a highly conductive graphitic framework that provides efficient electron transfer channels, while the encapsulation of active nanoparticles within CNTs effectively suppresses aggregation and dissolution during electrochemical operation [16, 17]. Furthermore, heteroatom doping into the carbon lattice, such as the co-incorporation of nitrogen (N) with sulfur (S), modifies the electronic structure, disrupts local charge neutrality, and tunes the adsorption energetics of reaction intermediates, collectively enhancing electrocatalytic activity [18]. For instance, Li et al. reported that S, N co-doped carbon nanotubes coupled with CoFe nanoparticles (CoFe/S−N−C) exhibited superior bifunctional ORR and OER performance, attributed to the synergistic interaction between the heteroatom dopants and the highly conductive carbon matrix [19].

Beyond interfacial and compositional engineering, rational nanostructure design, such as

porous, hollow, and yolk-shell architecture, has proven effective in enhancing mass transport under alkaline conditions [20, 21]. Among these, porous structures offer multiple advantages: enlarged surface areas ensure abundant exposure of active sites, while interconnected pore channels promote efficient ion diffusion and electrolyte penetration [22]. NaCl has recently gained considerable attention as a templating additive in the synthesis of porous carbon structures, owing to its ability to infiltrate precursors in the molten state and generate well-defined pore networks upon removal [23]. As a class of metal-organic frameworks (MOFs), Zeolitic imidazolate frameworks (ZIFs) are particularly attractive precursors for porous carbon synthesis due to their well-defined structures, tunable compositions, and intrinsic microporosity [24, 25]. However, during high-temperature pyrolysis, ZIF-derived carbons suffer from organic ligand decomposition and particle agglomeration. The introduction of molten salt-assisted carbonization effectively overcomes these limitations by preserving morphology and suppressing agglomeration [26]. As a representative example, Zhang et al. demonstrated that molten NaCl-assisted synthesis of Fe and Co co-modified N-doped porous carbon (FeCo-NHPC) derived from ZIF precursors delivered superior bifunctional catalytic activity, validating the effectiveness of the molten salt strategy in optimizing MOF-derived electrocatalysts [27].

Motivated by the above design rationale and to address the existing performance gaps, we report herein the synthesis of Co/CoS_2 heterostructures embedded within N,S dual-doped carbon nanotubes (Co/CoS_2/NSCNT) via a NaCl-assisted MOF-derived strategy, targeting high-performance bifunctional electrocatalysis for rechargeable ZABs in alkaline media. The Co/CoS_2/NSCNT electrocatalyst integrates several synergistic structural and electronic advantages: (1) NaCl-assisted synthesis enhances the specific surface area and effectively suppresses particle agglomeration during high-temperature pyrolysis; (2) in-situ grown CNTs on the nanoparticle surface construct a highly conductive three-dimensional network that

facilitates rapid electron transfer; (3) N and S co-doping induces change in the local electronic environment of the carbon framework, improving hydrophilicity and establishing an efficient solid-liquid-gas triple-phase boundary; and (4) the intimate Co/CoS_2 Mott-Schottky heterojunction accelerates charge transfer and optimizes intermediate adsorption energetics by generating a built-in electric field. Electrochemical evaluation revealed that Co/CoS_2/NSCNT achieves outstanding OER activity, with an overpotential of 334 mV at 10 mA cm^{-2} and a Tafel slope of 63.3 mV dec^{-1}. The catalyst also demonstrates remarkable ORR activity with a half-wave potential of 874 mV and a Tafel slope of 32.6 mV dec^{-1}, surpassing the benchmark Pt/C catalyst. This competitive performance leads to high-power density of 199.15 mW cm^{-2} as applied to the air cathode of AEMFC. When assembled into liquid-state and flexible ZABs, the devices deliver peak power densities of 163.57 and 95.19 mW cm^{-2}, respectively, along with robust cycling stability superior to that of the Pt/C + RuO_2 benchmark. This study presents a generalizable strategy for developing high-performance non-precious metal bifunctional electrocatalysts toward sustainable and efficient energy storage technologies.

2. Experimental section

2.1 Materials and chemicals

Cobalt(II) nitrate hexahydrate ($Co(NO_3)_2 \cdot 6H_2O$, 99.0%), zinc nitrate hexahydrate ($Zn(NO_3)_2 \cdot 6H_2O$, 99.0%), dicyandiamide ($C_2H_4N_4$), and thiourea (CH_4N_2S) were purchased from Sigma-Aldrich. 2-Methylimidazole ($C_4H_6N_2$, 98.0%) was acquired from TCI Chemicals. Sodium chloride (NaCl) was obtained from Duksan Pure Chemicals. All reagents were used directly without any additional purification.

2.2 Synthesis of Bimetallic Zn, Co-ZIF

Bimetallic Zn, Co-ZIF nanoparticles were synthesized based on a modified ZIF-67 preparation procedure. First, 892.5 mg of $Zn(NO_3)_2 \cdot 6H_2O$ (3 mmol) and 291.0 mg of $Co(NO_3)_2 \cdot 6H_2O$ (1 mmol) were dissolved in 30 mL of methanol (Solution A). Separately, 2000 mg of 2-methylimidazole (2-MeIM) was dissolved in 30 mL of methanol (Solution B). Both solutions were thoroughly stirred for 30 min and then combined. This mixture was continuously stirred for 3.5 h and subsequently aged at room temperature for 25 h. The precipitate was collected by centrifugation at 5000 rpm for 5 min, washed three times with methanol, and dried overnight at 60°C to yield the Zn, Co-ZIF precursor.

2.3 Synthesis of Co/NC

Co/NC was synthesized by thoroughly mixing Zn, Co-ZIF powder (150 mg) and NaCl (150 mg) using a vortex mixer to obtain a homogeneous mixture. The mixture was then pyrolyzed in a tube furnace at 900°C for 2 h under an Ar atmosphere at a heating rate of 5°C min^{-1}. The heat-treated product was washed with deionized water by centrifugation at 9000 rpm for 10 min to remove residual NaCl, and subsequently dried overnight to obtain NaCl-assisted Co/NC. For comparison, a NaCl-free reference sample (SF-Co/NC) was prepared following the identical procedure in the absence of NaCl.

2.4 Synthesis of Co/NCNT and Co/CoS_2/NSCNT

Co/CoS_2/NSCNT was prepared via a two-step vapor-phase deposition strategy. In the first step, 2500 mg of dicyandiamide (DCDA) and 25 mg of Co/NC were placed at the upstream and downstream positions of a tube furnace, respectively. The sample was pyrolyzed at 750°C for 1.5 h under Ar flow at a ramping rate of 2°C min^{-1} to yield Co/NCNT. For comparison, the salt-free control sample (SF-Co/NCNT) was synthesized following the identical pyrolysis procedure in the absence of NaCl assistance. In the second step, 4000 mg of thiourea and 20

mg of Co/NCNT were placed at the upstream and downstream positions of the tube furnace, respectively, and pyrolyzed at 450°C for 2 h under Ar flow at a ramping rate of 2°C min^{-1} to obtain the final product, Co/CoS_2/NSCNT. For comparison, a NaCl-free reference sample (SF-Co/CoS_2/NSCNT) was prepared following the identical pyrolysis procedure without NaCl assistance.

2.5 Physicochemical characterization

The phase composition and crystal structures of the synthesized materials were investigated by X-ray diffraction (XRD; RIGAKU, SmartLab; Inha University Core-Facility Center for Sustainable Energy Materials (CFSE) of Korea Basic Science Institute (KBSI)) using Cu-Kα radiation (λ=0.154 nm). Raman spectra were collected using a Raman spectrometer (HORIBA, LabRAM Revolution) with excitation light source of 532 nm wavelength to evaluate the degree of graphitization degree of carbon species. The specific surface area and pore size distribution were measured through Brunauer-Emmett-Teller (BET) and Barrett-Joyner-Halenda (BJH) analysis based on nitrogen adsorption-desorption isotherm at 77 K (ASAP 2020). The morphology of the samples were examined by field-emission scanning electron microscopy (FE-SEM; HITACHI, S-4300) and transmission electron microscopy (TEM; JEOL, JEM2100F) coupled with an energy dispersive spectroscopy (EDS). Surface charge properties of the prepared samples were measured using zeta potential analyzer (Malvern, Nano Zetasizer). Contact angle was measured using Data-physics instrument (DCAT 21). The elemental compositions and chemical states were analyszed using X-ray photoelectron spectroscopy (XPS; Thermo Scientific, K-Alpha) with monochromatic Al-Kα radiation (hν = 1486.6 eV).

2.6 Electrochemical half-cell test for ORR and OER

Conventional three-electrode setup using a Princeton Applied Research VSP potentiostat was used fot all electrochemical measurements. The rotating disk electrode (RDE) includes working electrode of a glassy carbon electrode (GCE), a graphite plate and a Hg/HgO electrode were used for the counter and the reference electrode, respectively. For the preparation of electrocatalyst ink, 2 mg of catalyst powder, 16 μL of a 5 wt% Nafion solution, 384 μL of deionized water, and 100 μL of isopropyl alcohol were mixed and followed by ultrasonic dispersion for 30 min. After the dispersion, 5 μL of the resulting homogeneous ink was drop-cast onto the surface of the GCE. Activation of the working electrode was achieved through 30 continuous cyclic voltammetry (CV) scans within the Faradaic potential window at a scan rate of 100 mV s^{-1}. The oxygen evolution reaction (OER) tests were performed in N_2-saturated 0.1 M KOH condition, whereas the oxygen reduction reaction (ORR) measurements were carried out in O_2-saturated 0.1 M KOH electrolyte. The electrocatalytic activity was evaluated using linear sweep voltammetry (LSV) at a scan rate of 5 mV s^{-1} under the same electrolyte saturation conditions. All LSV curves were modified with 85% iR-compensation. The measured potentials were converted to the reversible hydrogen electrode (RHE) scale based on the Nernst equation:

$$E_{RHE} = E_{Hg/HgO} + 0.0592 \times \mathrm{pH} + E^0_{Hg/HgO}$$

As the standard potential of the Hg/HgO electrode ($E^0_{Hg/HgO}$) was determined to be 0.098 V vs. RHE using a stable saturated calomel electrode (SCE). The electrons transfer number (n) for the ORR process was calculated from LSV polarization curves measured at various rotation speeds using the K–L equation:

$$\frac{1}{J} = \frac{1}{J_K} + \frac{1}{J_D}$$

$$J_K = nFkC_0$$

$$J_D = 0.62nFD^{3/2}v^{-1/6}\omega^{1/2}C_{O_2}$$

where J, J_K and J_D represents measured, kinetic, and diffusion-limiting current densities, respectively. For the two below equations, $J_K = nFkC_0$ and $J_D = 0.62nFD^{3/2}v^{-1/6}\omega^{1/2}C_{O_2}$, n represents the electron transfer number, F is the Faraday constant (96485 C mol^{-1}), k is the electron transfer rate constant, C_0 is the bulk concentration of O_2. D denotes the diffusion coefficient of O_2 in 0.1 M KOH (1.9×10^{-5} cm^2 s^{-1}), v is the kinematic viscosity (1.09×10^{-2} cm^2 s^{-1}), ω is the angular rotation rate, and C_{O_2} is the dissolved O_2 concentration in the electrolyte (1.2×10^{-6} mol cm^{-3}). Rotating ring-disk electrode (RRDE) measurements were carried out at a scan rate of 5 mV s^{-1} using the same catalyst ink composition used for RDE measurements. The electron transfer number (n) and peroxide yield (%HO_2^-) were calculated through the following equation:

$$n = 4 \times \frac{I_{disk}}{I_{ring}/N + I_{disk}}$$

$$\%HO_2^- = 200 \times \frac{I_{ring}/N}{I_{ring}/N + I_{disk}}$$

where I_{disk} and I_{ring} represents the disk and ring currents, and N is collection efficiency of the Pt ring (0.37). The electrochemical double-layer capacitance (C_{dl}) was calculated from CV measurements in the non-Faradaic potential region of 0.8–1.0 V vs. RHE at scan rates ranging from 20 to 100 mV s^{-1}. The C_{dl} value was gained from the slope of the linear plot between capacitive current density ($\Delta j = (j_{anodic} - j_{cathodic})/2$) and scan rate. The electrochemically active surface area (ECSA) was calculated by dividing C_{dl} by the specific capacitance C_S (40 μF cm^{-2} in alkaline media). The electrochemical impedance spectroscopy (EIS) analysis was carried out at a frequency range of 100 kHz to 100 mHz with 5 mV amplitude for charge-transfer resistance (R_{ct}) evaluation. The turnover frequency (TOF) was

determined using the following equation:

$$TOF = \frac{jA}{zFn}$$

where j is the current density (mA cm^{-2}) obtained from the LSV measurements, A is the geometric area of the GCE (0.0707 cm^2), z is the number of the transferred electrons (z = 4 for OER), F is the Faraday constant (96485 C mol^{-1}), and n stands for the number of active sites (mol). The n was estimated from CV measurements conducted in the non-Faradaic region (-0.2 to 0.6 V vs. RHE) at scan rate of 50 mV s^{-1} in 1.0 M phosphate-buffered saline (PBS, pH 7). The number of active sites (n) were calculated from the CV measurements in the phosphate buffered saline (PBS) at a non-Faradic potential region according to the following equation:

$$n = \frac{Q}{2F}$$

where, Q is the total charge from the CV measurement. The long-term durability of Co/CoS_2/NSCNT was evaluated using chronoamperometry (CA) at 0.7 V vs. RHE for ORR and 1.56 V vs. RHE for OER over 100 h. Tolerance for Methanol was measured by CA in O_2-saturated 0.1 M KOH containing 3 M methanol. Accelerated degradation test (ADT) was conducted by continuous 1000 cycle CV scanning within the potential range of 1.2–1.7 V vs. RHE at a scan rate of 100 mV s^{-1}.

2.7 Membrane electrode assembly (MEA) preparation and AEMFC testing

The catalyst was spray-coated onto the anion exchange membrane (AEM) by an active area of 5 cm^2, to fabricate the MEA. The membrane was pretreated in a 1.0 M KOH solution for 24 h ion exchange facilitation, prior to catalyst coating. The catalyst ink for the cathode electrode was prepared by mixing 13 mg of Co/CoS_2/NSCNT with 87 µL of anion exchange dispersion

(5 wt%, PiperION), 1.14 mL of deionized water, and 4.2 mL of isopropanol and sonicating for 2 h. The ink for the anode electrode was also prepared by sonicating the mixture of 7 mg of Pt/C, 48 μL of anion exchange dispersion, 6 mL of deionized water, and 2.2 mL of isopropanol. Subsequently the prepared catalyst ink was sprayed onto the pretreated AEM uniformly, and the coated membrane was soaked in 1.0 M KOH solution for the second time. The total loading amount of the cathode and the anode were 2.0 mg cm^{-2} of Co/CoS_2/NSCNT and 1.0 mg cm^{-2} for Pt/C, respectively. The MEA was assembled along with two PTFE gaskets and gas diffusion layers (GDL, Sigracet 39BB) on each side. The single fuel cell was assembled by the torque of 5 N·m using a torque wrench. The operation conditions for the fuel cell were 70°C and a flow rate of H_2/O_2 = 200/300 sccm, with 100% relative humidity (RH). The hydration of the membrane was induced by the high humidity condition, which leads to efficient ion transport and reduced resistance. The backpressure was not applied during the operation to prevent problems such as water flooding, catalyst detachment, and AEM degradation.

2.8 Fabrication and performance test of rechargeable quasi-solid-state flexible Zn-air battery

Quasi-solid-state rechargeable flexible ZAB was fabricated using a 0.2 mm-thick zinc foil for the anode and flexible carbon cloth substrate coated with catalyst loading of 1.0 mg cm^{-2} for the air cathode. The polyacrylic acid (PAA) hydrogel was applied as the polymer electrolyte, which was synthesized by mixing 1 g of acrylic acid (AA) with 10 mL of aqueous solution containing 0.5 M ZnO and 11.25 M KOH with vigorous stirring, followed by adding 100 mg of N,N′-methylene-bisacrylamide. Subsequently, 300 μL of 0.3 M $K_2S_2O_4$ (KPS) was introduced as an initiator, leading to rapid polymerization of the AA. The as-prepared PAA hydrogel was placed between the air cathode and zinc foil during the cell assembly, and the cell was sealed using two layers of packaging film for protection and leakage prevention of the

device. The same methods of electrochemical performance were used for of the flexible ZAB as for the liquid ZAB. For rate performance tests, the current density was changed from 1 to 5 mA cm^{-2}, while long-term cycling test was carried out at a constant current density of 2 mA cm^{-2}.

3. Results and Discussion

3.1 Synthetic procedure of Co/CoS_2/NSCNT

As illustrated in Scheme 1, Zn, Co-ZIF was synthesized via a co-precipitation method using Zn^{2+} and Co^{2+} ions with 2-methylimidazole as the organic ligand. The bimetallic ZIF powder was subsequently combined with NaCl through grinding and vortex mixing to synthesize a homogeneous precursor mixture. This resulting mixture was pyrolyzed at 900°C under an Ar atmosphere to yield Co/NC, a NaCl-assisted N-doped porous carbon. During pyrolysis, the thermal volatilization of Zn, driven by its relatively low boiling point and high vapor pressure, generates a mesoporous carbon framework [28]. Concurrently, the molten NaCl particles serve as sacrificial hard templates, and their removal upon washing creates interconnected mesopores, producing a synergistic porosity enhancement in conjunction with Zn evaporation. Furthermore, the molten NaCl encapsulates the ZIF precursor during carbonization, effectively preserving the dodecahedral morphology of the ZIF-derived carbon. Deionized water was used for the removal of residual NaCl from the obtained Co/NC and subsequently the dried powder was co-pyrolyzed with dicyandiamide (DCDA) under Ar flow at 750°C for 1.5 h to yield Co/NCNT. In this step, DCDA serves as both a nitrogen and carbon source, generating reactive intermediates including melamine and melem upon thermal decomposition and polymerization at elevated temperatures [29]. The subsequent carbonization of this polymeric network contributes to the N-doped carbon nanotubes (NCNTs) formation through catalytic

graphitization facilitated by the embedded metallic Co nanoparticles [30]. Finally, Co/NCNT was sulfurized with thiourea at 450°C for 2 h under Ar atmosphere, simultaneously inducing partial Co sulfurization to form Co/CoS_2 heterostructures and introducing sulfur species into the carbon framework to yield Co/CoS_2/NSCNT. The partial nature of sulfurization is attributed to the limited diffusion of sulfur vapor into the interior Co sites, which are encapsulated within the NCNTs, thereby preserving the metallic Co phase and enabling the formation of well-defined Co/CoS_2 heterointerfaces [31]. For comparison, SF-Co/CoS_2/NSCNT and CoS_2/NSC were synthesized following identical procedures but without molten salt-assisted pyrolysis and without the addition of DCDA, respectively.

3.2 Physicochemical characterization of electrocatalysts

X-ray diffraction (XRD) analysis was performed to identify the phase compositions and crystalline structures of the synthesized materials. Fig. S1 presents the XRD patterns of bimetallic Zn, Co-ZIF, ZIF-67, and ZIF-8. A noticeable shift of the diffraction peaks toward lower angles is observed for ZIF-8 relative to ZIF-67, which can be attributed from the larger ionic radius of Zn^{2+} (74 pm) compared to that of Co^{2+} (72 pm), resulsting in a slight expansion of the lattice parameters. Furthermore, the peak positions of the bimetallic Zn, Co-ZIF closely resemble those of ZIF-8 rather than ZIF-67, suggesting that the crystal structure of the mixed-metal ZIF is predominantly governed by the higher Zn^{2+} content relative to Co^{2+} [32]. Following thermal annealing of bimetallic Zn, Co-ZIF at 900°C, the XRD pattern of Co/NC (Fig. 1a) displays diffraction peaks at 44.2°, 51.5°, and 75.8°, indexed to (111), (200), and (220) planes of cubic metallic Co, respectively (JCPDS No. 01-089-7093) [33]. No diffraction peaks corresponding to Zn species were detected, consistent with the complete evaporation of Zn at the pyrolysis temperature. Upon subsequent annealing of Co/NC in the presence of DCDA, the XRD pattern of Co/NCNT retains the characteristic diffraction peaks of metallic Co. In

addition, a broad diffraction peak near 26.5° is attributed to the (002) plane of graphitic carbon [34]. The absence of this peak in Co/NC and its emergence in Co/NCNT strongly supports the formation of CNT structures, consistent with the well-established role of metallic Co nanoparticles as catalytic centers for CNT growth during high-temperature annealing [30].

After partial sulfidation, the XRD pattern of Co/CoS_2/NSCNT reveals additional diffraction peaks at 27.9°, 32.3°, 36.2°, 39.8°, 46.6°, and 54.9°, assigned to the (111), (200), (210), (211), (220), and (311) planes of CoS_2, respectively (JCPDS No. 00-041-1471) [35]. The coexistence of characteristic diffraction peaks corresponding to both metallic Co and CoS_2 confirms the successful construction of a Co/CoS_2 heterointerface through controlled sulfurization of the Co/NCNT precursor. Conversely, the XRD pattern of the CoS_2/NSC reference catalyst shows complete conversion of metallic Co to CoS_2, as evidenced by the disappearance of metallic Co peaks, along with the absence of the graphitic carbon peak near 26.5°. The latter observation indicates the formation of amorphous carbon rather than CNT structures in the absence of DCDA, while the complete sulfidation highlights the critical role of CNT encapsulation in stabilizing the metallic Co phase and enabling the formation of a well-defined Co/CoS_2 heterostructure [31]. Additionally, the XRD pattern of SF-Co/CoS_2/NSCNT exhibits comparatively lower CoS_2 peak intensities relative to Co/CoS_2/NSCNT. This phenomenon originates from the agglomeration of Co nanoparticles in the absence of NaCl-assisted synthesis, which increases the average particle size and retards sulfidation kinetics through diffusion-limited sulfide species transport, ultimately resulting in a lower CoS_2-to-metallic Co intensity ratio [26, 36].

Raman spectroscopy was employed to evaluate the chemical structure and defect characteristics of the synthesized samples (Fig. 1b). Two prominent bands are observed at approximately 1340 and 1590 cm^{-1}, corresponding to the D band (A_{1g} vibration mode of disordered carbon) and the G band (E_{2g} vibration mode of graphitic carbon), respectively [37].

The D band to G band intensity ratio (I_D/I_G) provides a quantitative measurement of structural disorder and defect density within the carbon framework, where higher values indicate a greater degree of defect sites, typically arising from heteroatom incorporation and lattice distortions [38]. The I_D/I_G values for Co/NC, Co/NCNT, CoS_2/NSC, SF-Co/CoS_2/NSCNT, and Co/CoS_2/NSCNT were determined as 0.86, 0.82, 0.84, 0.91, and 1.11, respectively. Notably, Co/CoS_2/NSCNT exhibits the highest I_D/I_G ratio among all samples, indicating the richest defect density generated by effective N, S co-doping into the carbon network. Such defect-rich carbon structures are widely recognized to promote reactant adsorption in aqueous electrolytes, resulting in acceleration of reaction kinetics and electrocatalytic activity enhancement toward both ORR and OER [39]. Comparative Raman analysis before and after sulfidation (Fig. S2) provides further evidence for successful sulfurization of Co/NCNT. A distinct Raman feature emerging at approximately 670 cm^{-1} in Co/CoS_2/NSCNT is consistent with the symmetric A_{1g} vibrational mode of cobalt sulfide [40], and its appearance, corroborated by the XRD results, collectively confirms the successful incorporation of sulfide species.

The specific surface area and pore characteristics of Co/NC, Co/NCNT, CoS_2/NSC, SF-Co/CoS_2/NSCNT, and Co/CoS_2/NSCNT were examined by N_2 adsorption-desorption measurements conducted at 77 K. As presented in Fig. 1c, Co/NC, Co/NCNT, SF-Co/CoS_2/NSCNT, and Co/CoS_2/NSCNT display type-IV isotherms accompanied by pronounced hysteresis loops in the 0.5-1.0 relative pressure (P/P_0) range, whereas CoS_2/NSC exhibits negligible hysteresis behavior. These observations indicate the presence of well-developed mesoporous structures arising from high-temperature pyrolysis and CNT formation, which collectively contribute to increased active site exposure and facilitate mass transport in aqueous electrolyte media [41]. The Brunauer-Emmett-Teller (BET) specific surface areas of Co/NC, Co/NCNT, CoS_2/NSC, SF-Co/CoS_2/NSCNT, and Co/CoS_2/NSCNT were determined to be 385.16, 197.41, 90.03, 155.14, and 255.68 $m^2\ g^{-1}$, respectively. The corresponding total

pore volumes, derived from the pore size distribution curves (Fig. 1d), were calculated to be 0.12, 0.25, 0.13, 0.26, and 0.49 cm^3 g^{-1} for Co/NC, Co/NCNT, CoS_2/NSC, SF-Co/CoS_2/NSCNT, and Co/CoS_2/NSCNT, respectively. Notably, Co/CoS_2/NSCNT exhibits a significantly higher specific surface area and larger total pore volume compared to its NaCl-free counterpart SF-Co/CoS_2/NSCNT, confirming that NaCl-assisted carbonization effectively promotes porous structure development and enlarges the electrochemically accessible surface area [23]. Although the BET specific surface area decreases after CNT growth, the pore size distribution shifts from a dominant pore diameter of approximately 2 nm to 4 nm, which is attributed to the elimination of fine micropores and the generation of interstitial voids formed during CNT growth on the particle surface. Following sulfidation, the volume of the total pores increases while the dominant pore diameter remains nearly unchanged, suggesting that the structural defects introduced during high-temperature sulfurization contribute to additional pore generation without significantly altering the pore size distribution [42]. Collectively, these results demonstrate that the integration of CNT networks and subsequent sulfidation synergistically modulate the pore architecture of Co/CoS_2/NSCNT, promoting mesoporous features that are highly favorable for electrolyte penetration and mass transport during electrochemical reactions [43]. To further elucidate the role of NaCl-assisted synthesis during carbonization, the BET specific surface areas of SF-Co/NC and SF-Co/NCNT were measured as 200.31 and 75.03 m^2 g^{-1} (Fig. S3a), with corresponding total pore volumes of 0.23 and 0.09 cm^3 g^{-1} (Fig. S3b), respectively. These values are substantially reduced compared to those of Co/NC and Co/NCNT, providing additional evidence that NaCl-assisted synthesis plays a critical role in developing a well-defined porous carbon framework.

The surface morphologies and mesostructures of the synthesized samples were examined by scanning electron microscopy (SEM) and transmission electron microscopy (TEM). As shown in Figs. 2a and 2e, Zn, Co-ZIF particles with a well-defined rhombic dodecahedral morphology

were successfully synthesized. Following NaCl-assisted carbonization, residual NaCl species were observed on the particle surface (Fig. S4), which were subsequently removed by repeated washing with deionized water. The resulting Co/NC retained the rhombic dodecahedral morphology with a highly porous surface (Figs. 2b and 2f), confirming that the combined effects of sacrificial NaCl templating and Zn evaporation effectively suppress particle agglomeration and promote the development of well-defined porous structures, which are expected to reduce ion diffusion distances and enhance the accessible electrochemically active surface area [23, 26, 28]. As shown in Figs. 2c and 2g, Co/NCNT exhibits a dense network of CNTs grown on the surface of the rhombic dodecahedral particles, providing efficient electron transport pathways and enhanced electrical conductivity. For comparison, SF-Co/NC and SF-Co/NCNT were synthesized to verify the role of NaCl during carbonization. Both samples exhibited significant morphology distortion and particle agglomeration due to thermal stress in the absence of NaCl (Figs. S5a and S5b), further corroborating the morphology-preserving function of the molten salt template.

Following high-temperature sulfidation, surface reconstruction of the dodecahedral particles is observed in Co/CoS_2/NSCNT (Figs. 2d and 2h). Similar surface reconstruction behavior has been widely observed in transition metal sulfide electrocatalysts, where thermally induced surface phase transformations contribute to catalytic activity modulation [44]. In contrast, the CoS_2/NSC reference sample (Fig. S6), synthesized without DCDA, shows no CNT growth on the particle surface and exhibits noticeable shrinkage of the particle diameter during pyrolysis. Similarly, SF-Co/CoS_2/NSCNT (Fig. S7), prepared without NaCl assistance, displays severe collapse of the dodecahedral structure and the growth of CNTs with abnormally large diameters, attributable to the agglomeration of Co nanoparticles during carbonization in the absence of the salt template. As shown in Fig. S10, Co nanoparticles are fully encapsulated within the

NSCNT shell, which is expected to confer excellent electrochemical stability by preventing nanoparticle aggregation and dissolution during prolonged cycling [17].

The high-resolution TEM (HRTEM) image of Co/CoS_2/NSCNT (Fig. 2i) clearly reveals the presence of graphitic carbon layers and well-defined Co/CoS_2 heterointerfaces. Selected area electron diffraction (SAED) analysis of Co/CoS_2/NSCNT (inset of Fig. 2i) shows distinct diffraction rings corresponding to the (111) and (210) planes of CoS_2 and the (111) plane of metallic Co, confirming the coexistence of both phases [45, 46]. Fast Fourier transform (FFT) and inverse FFT (IFFT) analyses of the marked regions 1 and 2 in Fig. 2i are presented in Figs. 2j and 2k, respectively. The lattice fringe spacing of region 1 is measured as 0.254 nm, corresponding to the (210) plane of CoS_2, while that of region 2 is determined as 0.202 nm, indexed to the (111) plane of metallic Co. The intimate contact between metallic Co and CoS_2 at the heterointerface introduces lattice mismatch and structural irregularities, generating abundant defect sites that effectively modulate electronic interactions with oxygen-containing reaction intermediates during electrocatalysis [13]. Energy dispersive X-ray spectroscopy (EDS) elemental mapping of Co/CoS_2/NSCNT (Figs. 2l-p) reveals the uniform spatial distribution of Co, S, N, and C throughout the composite, confirming the successful and homogeneous incorporation of N and S dopants into the carbon matrix. Quantitative EDS analysis yields atomic percentages of 0.49, 1.19, 2.27, and 96.05% for Co, S, N, and C, respectively.

To examine the effect of sulfidation on the surface properties of the synthesized catalysts, zeta potential for Co/NCNT, SF-Co/CoS_2/NSCNT, and Co/CoS_2/NSCNT were measured as dispersed in deionized water. As shown in Fig. S11, Co/CoS_2/NSCNT exhibits the most positive zeta potential value (30.36 mV) among the three samples, exceeding those of Co/NCNT (19.72 mV) and SF-Co/CoS_2/NSCNT (26.51 mV), indicating a highly positive surface charge. The progressive shift toward a more positive surface charge following

sulfidation can be ascribed to the introduction of sulfur components with high electron affinity, which increases surface polarity [47]. Effective electrolyte transport to the three-phase boundary of the air cathode is a critical factor governing the performance of rechargeable Zn-air batteries, and surface charge characteristics play an important role in determining this transport behavior [48]. Enhanced surface hydrophilicity facilitates electrolyte penetration into the porous electrode structure, thereby alleviating mass transport limitations and improving electrocatalytic activity in aqueous media [49].

As evidenced by contact angle measurements (Fig. S12a-d), Co/CoS_2/NSCNT-coated carbon cloth exhibits a substantially reduced contact angle of 73.2° relative to bare carbon cloth (128.1°), Co/NCNT-coated carbon cloth (103.9°), and SF-Co/CoS_2/NSCNT-coated carbon cloth (99.7°), demonstrating significantly enhanced surface wettability. This improvement is primarily attributed to the increased surface polarity introduced by sulfur incorporation. Furthermore, the higher surface polarity of Co/CoS_2/NSCNT compared to SF-Co/CoS_2/NSCNT is ascribed to the more extensive degree of sulfidation achieved through NaCl-assisted synthesis, which collectively contributes to enhanced electrolyte wettability and improved reactant accessibility at the electrode-electrolyte interface during electrochemical reactions [50].

To elucidate the chemical composition and electronic environment of the synthesized catalysts (CoS_2/NSC, Co/NCNT, and Co/CoS_2/NSCNT), X-ray photoelectron spectroscopy (XPS) was performed. The XPS survey spectra of all three samples are consistent with the EDS results (Fig. S13). The high-resolution Co 2p spectra (Fig. 3a) were deconvoluted into distinct electronic states. Specifically, the peaks at 782.31 and 797.15 eV are assigned to Co^{2+}, as those at 780.15 and 795.46 eV correspond to Co^{3+} species. The presence of metallic cobalt (Co^0) is evidenced by peaks at 778.34 and 793.69 eV [51]. Notably, the absence of Co^0 signals in CoS_2/NSC indicates complete phase conversion from metallic Co to CoS_2 during sulfidation,

consistent with the XRD results. Furthermore, both sulfurized catalysts exhibit a positive shift in the Co^{2+} and Co^{3+} binding energies relative to Co/NCNT, which can be ascribed to the incorporated sulfur components' electron-withdrawing effect that modifies the local electronic structure of Co [52]. The more pronounced positive shift observed in Co/CoS_2/NSCNT compared to CoS_2/NSC further indicates directional electron flow from the metallic Co core to the CoS_2 phase across the Mott-Schottky heterojunction [46].

The high-resolution S 2p spectra (Fig. 3b) provide further evidence of electronic redistribution at the Co/CoS_2 heterointerface. The four deconvoluted peaks at 162.80, 163.93, 164.79, and 168.78 eV are assigned to S $2p_{3/2}$ and S $2p_{1/2}$ of cobalt-sulfur bonds, carbon-incorporated sulfur species (C−S−C), and surface-oxidized sulfur species (SO_x), respectively [53]. Compared to those of CoS_2/NSC, the metal-sulfur binding energies of Co/CoS_2/NSCNT are shifted to lower values, corroborating efficient electron transfer across the metal-semiconductor interface of the Mott-Schottky junction and confirming the accumulation of electron density at sulfur sites [54].

The high-resolution N 1s spectra (Fig. 3c) reveal four characteristic peaks at binding energies of 398.41, 400.15, 401.29, and 403.12 eV, corresponding to pyridinic N, pyrrolic N, graphitic N, and oxidized N, respectively [55]. These results confirm that nitrogen species were effectively introduced into the carbon structure, generating numerous defect sites that serve as active centers for reactant adsorption during both ORR and OER [56]. Notably, Co/CoS_2/NSCNT exhibits a marked increase in pyridinic N peak intensity relative to Co/NCNT, suggesting that high-temperature sulfidation promotes the structural rearrangement of nitrogen dopants into the more thermodynamically stable pyridinic N configuration. Pyridinic N is recognized to act synergistically with graphitic N by providing optimized adsorption sites with enriched lone-pair electron density, effectively lowering the energy barriers for oxygen intermediate adsorption during ORR [57].

In Fig. 3d, five components at 283.38, 284.78, 285.64, 286.30, and 288.61 eV, assigned to Co−C, C−C, C=N, C−S, and C=O bonds, respectively, were deconvoluted from the high-resolution C 1s spectra [58–60]. The coexistence of C=N and C−S bonds confirms the successful dual doping of nitrogen and sulfur into the carbon framework [61]. Such heteroatom doping, involving elements with contrasting electronegativities, enhances surface polarity and strengthens the chemical interaction with oxygen intermediates during electrocatalysis [18]. Additionally, a weak and broad peak observed at 290.95 eV in both Co/NCNT and Co/CoS_2/NSCNT corresponds to the π to π* transition, characteristic of the sp_2-hybridized graphitic carbon framework associated with CNT network formation [62].

To further elucidate the synergistic electronic effects at the heterointerface, the band alignment between metallic Co and CoS_2 was evaluated based on their respective work functions of 5.0 and 5.5 eV (Figs. 3e and 3f) [63, 64]. Since the n-type semiconductor CoS_2 has a higher work function than the metallic Co, a Mott-Schottky junction is spontaneously established upon contact, driving directional electron migration from Co to CoS_2 and generating a built-in electric field at the interface that significantly accelerates charge transfer kinetics [12, 65]. As a result, the electrophilic Co sites effectively stabilize oxygen adsorbates, while the electron-enriched CoS_2 regions lower the energy barriers for intermediate adsorption and desorption, synergistically enhancing both ORR and OER behavior [66]. In summary, the superior bifunctional electrocatalytic performance of prepared catalyst originates from the strong electronic coupling and optimized charge distribution established within the Mott-Schottky heterojunction, in concert with the synergistic contributions of N, S dual-doping and the hierarchical porous CNT architecture.

3.3 Electrocatalytic OER performance of electrocatalysts

The OER activities of the as-synthesized electrocatalysts and commercial RuO_2 were evaluated in N_2-saturated 0.1 M KOH electrolyte. As depicted in Fig. 4a, linear sweep voltammetry (LSV) polarization curves were recorded with 85% iR compensation at a scan rate of 5 mV s^{-1}. Co/CoS_2/NSCNT achieves a current density of 10 mA cm^{-2} at an overpotential of 334 mV, outperforming Co/NC (425 mV), Co/NCNT (396 mV), CoS_2/NSC (400 mV), and SF-Co/CoS_2/NSCNT (385 mV). For further assessment of catalytic kinetics, Tafel slopes were derived from the corresponding LSV curves (Fig. 4b). The Tafel slopes for Co/NC, Co/NCNT, CoS2/NSC, SF-Co/CoS_2/NSCNT, Co/CoS_2/NSCNT, and RuO_2 were determined to be 83.03, 74.88, 83.66, 99.91, 63.34, and 80.04 mV dec^{-1}, respectively. Although RuO_2 exhibits a similar overpotential at 10 mA cm^{-2} (332 mV vs. 334 mV for Co/CoS_2/NSCNT), Co/CoS_2/NSCNT requires a significantly lower overpotential of 419 mV compared to RuO_2 (496 mV) at a high current density of 100 mA cm^{-2}, consistent with its remarkably low Tafel slope and superior intrinsic charge transfer kinetics. These results indicate that the synergistic effects of N, S dual-heteroatom doping and Mott-Schottky junction formation effectively modify the surface electronic properties of the catalyst, enhancing OH^- adsorption at the active sites and facilitating the rate-determining step of OER [67, 68]. A comprehensive comparison of overpotentials and Tafel slopes summarized in Table S2 confirms that Co/CoS_2/NSCNT surpasses many previously reported non-precious metal electrocatalysts for OER.

To assess intrinsic catalytic efficiency, turnover frequency (TOF) values were calculated from the LSV data across the entire potential range (Fig. 4c). The TOF of Co/CoS_2/NSCNT at 1.7 V vs. RHE (9.06 s^{-1}) substantially exceeds those of Co/NC (1.31 s^{-1}), Co/NCNT (2.83 s^{-1}), CoS_2/NSC (2.16 s^{-1}), and SF-Co/CoS_2/NSCNT (4.41 s^{-1}), confirming its superior intrinsic catalytic activity on a per-active-site basis. Collectively, the LSV, Tafel slope, and TOF results consistently demonstrate that Co/CoS_2/NSCNT possesses outstanding intrinsic OER activity, characterized by low overpotential and favorable reaction kinetics.

The charge-transfer behavior of the electrodes was investigated by electrochemical impedance spectroscopy at an applied potential of 1.65 V versus RHE over frequencies ranging from 100 kHz to 100 mHz (Fig. 4d). The impedance response was interpreted using a Randles-based circuit model (Fig. S14), where the fitting parameters included the electrolyte resistance (R_s), charge-transfer resistance (R_{ct}), and constant phase element (CPE). The R_{ct} values of Co/NC, Co/NCNT, CoS_2/NSC, SF-Co/CoS_2/NSCNT, and Co/CoS_2/NSCNT were determined to be 33, 27, 31, 25, and 9 Ω, respectively. The lowest R_{ct} of Co/CoS_2/NSCNT indicates substantially enhanced charge transfer kinetics, mainly arising from the synergistic contribution of the conductive CNT network and numerous heterointerfaces that generate built-in electric fields and facilitate rapid electron migration during OER [12, 16].

The electrochemically active surface area (ECSA) was estimated from cyclic voltammetry (CV) curves recorded within the non-faradaic potential region (0.8-1.0 V vs. RHE) at various scan rates (Fig. S15a-e). The double-layer capacitance (C_{dl}) was determined from the linear relationship between the current density difference ($\Delta j = (j_a - j_c)/2$) at 0.9 V vs. RHE and the scan rate, and the ECSA was calculated according to the equation below:

$$ECSA = \frac{C_{dl}\ of\ electrocatalyst\ (mF\ cm^{-2})}{average\ specific\ capacitance\ (0.04\ mF\ cm^{-2})}$$

, where 0.04 mF cm^{-2} is a commonly employed value for the alkaline electrolyte average specific capacitance (C_s). As shown in Fig. 4e, Co/CoS_2/NSCNT exhibits the highest C_{dl} value of 24.12 mF cm^{-2}, substantially exceeding those of Co/NC (4.35 mF cm^{-2}), Co/NCNT (12.06 mF cm^{-2}), CoS_2/NSC (9.09 mF cm^{-2}), and SF-Co/CoS_2/NSCNT (17.52 mF cm^{-2}). This substantial enhancement in C_{dl} indicates a significantly enlarged electrochemically accessible active surface area, likely arising from the abundant defect sites generated by heterointerface formation, which promote reactant adsorption during OER [10, 22].

In Fig. 4f, chronoamperometry (CA) tests were conducted in N_2-saturated 0.1 M KOH and

at a fixed potential of 1.56 V vs. RHE to evaluate long-term durability. Remarkably, after 100 h of continuous OER operation, Co/CoS_2/NSCNT maintained 97.72% of the original current response, clearly exceeding the stability of RuO_2 (84.88%). Accelerated degradation test (ADT) was additionally performed over 1000 CV cycles between 1.4 and 1.75 V at a scan rate of 100 mV s^{-1}. The post-ADT LSV curve exhibited negligible performance degradation, further confirming the outstanding electrochemical stability of the developed catalyst. The exceptional durability can be ascribed to the protective CNT shells, which effectively prevent the encapsulated Co-based nanoparticles from aggregation and dissolution under prolonged alkaline operation [17].

3.4 Electrocatalytic ORR performance of electrocatalysts

The electrocatalytic ORR performances of Co/NC, Co/NCNT, CoS_2/NSC, SF-Co/CoS_2/NSCNT, and Co/CoS_2/NSCNT were evaluated in a conventional three-electrode setup using a rotating disk electrode (RDE) in O_2-saturated 0.1 M KOH electrolyte. Cyclic voltammetry (CV) was first conducted under both N_2- and O_2-saturated conditions within the potential window of 0.2-1.3 V vs. RHE at a scan rate of 5 mV s^{-1} without RDE rotation (Fig. 5a). No redox peaks were observed for all catalysts under N_2-saturated conditions. In contrast, under O_2-saturated conditions, well-defined cathodic peaks emerged, with Co/CoS_2/NSCNT exhibiting the highest peak potential (0.79 V vs. RHE) among all samples, surpassing Co/NC (0.74 V), Co/NCNT (0.76 V), CoS_2/NSC (0.73 V), and SF-Co/CoS_2/NSCNT (0.74 V), indicative of superior ORR activity in alkaline media. Furthermore, the quasi-rectangular CV area of the Co/CoS_2/NSCNT was the largest under N_2-saturated conditions, consistent with its highest double-layer capacitance and largest electrochemically active surface area.

To further probe the ORR kinetics, LSV measurements were performed at a scan rate of 5 mV s^{-1} and a rotation speed of 1600 rpm (Fig. 5b). Co/CoS_2/NSCNT achieves the highest half-

wave potential of 0.874 V vs. RHE, surpassing Co/NC (0.813 V), Co/NCNT (0.831 V), CoS_2/NSC (0.815 V), SF-Co/CoS_2/NSCNT (0.827 V), and commercial Pt/C (0.845 V). Its limiting current density of 5.98 mA cm^{-2} also exceeds that of Pt/C (5.90 mA cm^{-2}), indicating excellent mass transport characteristics. Intrinsic ORR kinetics were further assessed through Tafel slope analysis derived from the LSV data (Fig. 5c). Co/CoS_2/NSCNT exhibits a markedly lower Tafel slope of 32.63 mV dec^{-1} compared to Co/NC (40.21 mV dec^{-1}), Co/NCNT (39.05 mV dec^{-1}), CoS_2/NSC (50.63 mV dec^{-1}), SF-Co/CoS_2/NSCNT (58.49 mV dec^{-1}), and commercial Pt/C (55.68 mV dec^{-1}), reflecting exceptionally favorable ORR kinetics. The synergistic integration of the mesoporous carbon framework derived from NaCl-assisted synthesis, the conductive CNT network facilitating efficient gas molecule transport [43], and the strong electronic coupling between the Co/CoS_2 heterostructure and the N, S dual-doped carbon framework, which collectively optimize charge transport and enhance intrinsic catalytic activity of Co/CoS_2/NSCNT are the primary contributors to the outstanding ORR performance [69]. As summarized in Table S3, the Tafel slope and the half-wave potential of Co/CoS_2/NSCNT are compared favorably with those of previously reported transition metal-based ORR electrocatalysts.

The ORR reaction pathway and electron transfer number (n) were analyzed using Koutecky-Levich (K-L) plots derived from LSV curves recorded at rotation speeds of 400-2025 rpm (Figs. 5d and S16a-h). The current density inverse (J^{-1}) was plotted against $\omega^{-1/2}$ at distinct potentials of 0.5-0.65 V, yielding an electron transfer number of n = 3.99 for Co/CoS_2/NSCNT, exceeding those of Co/NC (3.76), Co/NCNT (3.85), CoS_2/NSC (3.87), and SF-Co/CoS_2/NSCNT (3.77). This value confirms that Co/CoS_2/NSCNT catalyzes oxygen reduction predominantly through a highly selective four-electron pathway, producing OH^- with minimal peroxide (HO_2^-) byproduct formation. Rotating ring-disk electrode (RRDE) measurements conducted at 1600 rpm were additionally employed for the peroxide yield quantification and the electron pathway

verification (Fig. S17b). Co/CoS_2/NSCNT exhibited an exceptionally low peroxide yield of approximately 2.04% and an n value of 3.97 over the potential range of 0.45-0.65 V vs. RHE, confirming near-ideal four-electron pathway selectivity with minimal HO_2^- production, in excellent agreement with the K-L analysis [70].

Long-term stability and methanol tolerance were also evaluated to assess the practical durability of Co/CoS_2/NSCNT. Conducted at 0.7 V vs. RHE for 100 h, CA measurements (Fig. 5e) demonstrate that Co/CoS_2/NSCNT retained 98.73% of its initial current density, whereas commercial Pt/C suffered a substantial decline of 21.13%, highlighting the markedly superior durability of Co/CoS_2/NSCNT. ADT carried out over 1000 CV cycles between 0.55 and 1.1 V at 100 mV s^{-1} resulted in negligible performance loss (Fig. S18), further verifying the strong structural robustness of the catalyst under accelerated electrochemical stress. Moreover, upon 3.0 M methanol injection during CA operation, Co/CoS_2/NSCNT maintained its ORR current with minimal disturbance, demonstrating excellent methanol tolerance, while Pt/C underwent a drastic deterioration in activity. These results collectively confirm that the protective NSCNT shell effectively stabilizes the encapsulated transition-metal active species and imparts strong resistance to methanol crossover, enabling reliable long-term ORR performance [17].

For further demonstration of the practical applicability of the developed electrocatalyst, an anion exchange membrane fuel cell (AEMFC) was fabricated including a polymeric AEM with a thickness of 20 μm. Commercial Pt/C and Co/CoS_2/NSCNT were utilized as the anodic and cathodic catalysts, respectively, with catalyst loadings of 1 and 2 mg cm^{-2}. All measurements were carried out at 75°C under fully humidified conditions (100% RH). The polarization curves and corresponding power density profiles are presented in Fig. 5h. The AEMFC incorporating the Co/CoS_2/NSCNT cathode delivered an OCV of 1.04 V and achieved a high peak power density of 199.15 mW cm^{-2} at a current density of 425.54 mA cm^{-2}. These values exceed those obtained with a commercial Pt/C cathode, which exhibited an OCV of 1.03 V and a peak power

density of 169.48 mW cm^{-2} at 391.41 mA cm^{-2}. These results clearly show that the prepared electrocatalyst functions effectively for ORR under AEMFC operating conditions and outperforms not only noble metal benchmarks but also previously reported non-precious cathode materials summarized in Table S4.

The AEMFC's operational durability was investigated by a 200 mA cm^{-2} constant-current stability test under 75°C, 100% RH, for 80 h (Fig. 5i). Both the Co/CoS_2/NSCNT-based and Pt/C-based cells exhibited an initial cell voltage of approximately 0.69 V. During prolonged operation, the Co/CoS_2/NSCNT-based AEMFC experienced a gradual voltage decay of approximately 0.18 V after 80 h, whereas the Pt/C-based cell suffered a substantially larger voltage loss of approximately 0.21 V within only 15 h of operation. The markedly slower voltage degradation observed for the Co/CoS_2/NSCNT cathode underscores its superior electrochemical robustness and highlights its excellent long-term durability under realistic AEMFC conditions.

The overall bifunctional oxygen electrocatalytic activity was quantified by calculating the potential gap (ΔE) between the OER potential at 10 mA cm^{-2} ($E_{j=10}$) and the ORR half-wave potential ($E_{1/2}$), as shown in Fig. 5f. Co/CoS_2/NSCNT displayed the smallest ΔE of 0.69 V among all evaluated samples, significantly lower than Co/NC (0.84 V), Co/NCNT (0.80 V), CoS_2/NSC (0.83 V), SF-Co/CoS_2/NSCNT (0.78 V), and the Pt/C + RuO_2 benchmark (0.72 V), along with many previously reported non-precious bifunctional electrocatalysts (Figs. S19a and S19b). This exceptionally narrow ΔE value underscores the outstanding overall oxygen electrocatalytic performance of Co/CoS_2/NSCNT and highlights its strong potential for practical utilization of rechargeable ZAB.

3.5 Optimization of Synthetic Conditions for Co/CoS_2/NSCNT

The bimetallic Zn, Co-ZIF was pyrolyzed with NaCl under temperatures ranging from 850 to 950°C to investigate the effect of calcination temperatures on the physicochemical properties of the Co/NC precursor. SEM observations (Fig. S20) revealed that pyrolysis at 950°C resulted in morphological collapse due to excessive thermal stress, whereas the dodecahedral structure was well preserved at both 850 and 900°C. TEM-EDS analysis (Fig. S21) further demonstrated that Zn was not completely removed at 850°C, confirming that full Zn evaporation is achieved at 900°C [71]. Accordingly, the carbonization temperature of 900°C was established as optimal for the synthesis of the Co/NC.

Following NaCl removal, Co/NC-900 was co-pyrolyzed with DCDA positioned upstream of the tube furnace for the formation of Co/NCNT. SEM observations (Fig. S22) reveal that the density of CNTs grown on the nanoparticle surfaces progressively increased with rising annealing temperature. At 650°C, CNT growth was negligible, likely due to insufficient thermal energy to drive the stepwise decomposition and catalytic graphitization of DCDA. Conversely, annealing temperatures exceeding 800°C led to morphological collapse and deterioration of the dodecahedral nanoparticle structure. The temperature-dependent structural evolution of the carbon framework was further examined by Raman spectroscopy (Fig. S23). No discernible D or G band features were observed below 700°C, indicating incomplete carbonization and CNT growth under insufficient thermal conditions. Beyond 750°C, the progressive increase in the D and G bands intensities can be attributed to enhanced catalytic decomposition of the DCDA precursor and increased nitrogen dopant incorporation, resulting in simultaneous advancement of graphitization and defect generation [72].

Comprehensive electrochemical evaluations for ORR and OER, including LSV, Tafel slope analysis, K-L analysis, EIS, and non-faradaic CV for C_{dl} determination, demonstrated that Co/NCNT-750 delivered the most favorable bifunctional activity among the temperature series (Figs. S24-27). These results establish 750°C as the optimal annealing temperature for

Co/NCNT synthesis, enabling the formation of well-graphitized NCNT structures while preserving the dodecahedral morphology.

To identify the optimal sulfidation conditions for Co/CoS_2/NSCNT synthesis, Co/NCNT-750 was subjected to thermal annealing with thiourea over a temperature range of 350 to 550°C. SEM analysis (Fig. S28) confirmed that the dodecahedral morphology decorated with CNTs remained largely intact across all sulfidation temperatures. Structural evolution during sulfidation was systematically examined by XRD (Fig. S29). Above 400°C, the diffraction peaks corresponding to metallic Cobalt progressively diminished, indicative of its gradual conversion to CoS_2. However, at 500 and 550°C, additional diffraction peaks at 30.7°, 35.4°, and 47° emerged, indexed to the (100), (101), and (102) planes of hexagonal CoS (JCPDS No. 03-065-3418) [73], indicating partial decomposition of sulfur species and thermally induced phase reconstruction at excessive temperatures. The formation of CoS is undesirable, as it diminishes intrinsic catalytic activity toward oxygen-related reactions and disrupts the interfacial electronic structure essential for efficient charge transfer [74]. Comprehensive electrochemical evaluation, including LSV, K-L plots, EIS, and C_{dl} estimation (Figs. S30-34), confirmed that Co/CoS_2/NSCNT-450 exhibited the highest bifunctional activity for both reactions among all tested sulfidation temperatures. This excellent performance at 450°C is primarily attributed to sufficient sulfur incorporation and the formation of well-defined Co/CoS_2 heterointerfaces, without the generation of undesirable impurity phases. Accordingly, Co/CoS_2/NSCNT-450 was selected as the optimal catalyst for the air cathode in the assembly of AEMFCs and rechargeable ZABs.

3.6 Application on liquid-state and flexible rechargeable Zn–air battery

To assess the practical feasibility of Co/CoS_2/NSCNT as a cathode material toward rechargeable Zn-air battery (ZAB) applications, a full ZAB cell was assembled using a zinc plate as the anode and Co/CoS_2/NSCNT-coated carbon cloth (CC) as the air cathode. A mixed electrolyte containing 6.0 M KOH and 0.2 M $Zn(CH_3COO)_2 \cdot 2H_2O$ was employed throughout the electrochemical measurements. A reference ZAB employing a Pt/C and RuO_2 mixed cathode (mass ratio 1:1) was measured under identical conditions for benchmarking. As illustrated in Fig. 6a, after 2000 s the Co/CoS_2/NSCNT-based ZAB displays a stable OCV of 1.50 V, approaching the theoretical voltage of 1.65 V and exceeding that of the benchmark cell (1.47 V). This improvement can be ascribed to the large surface area and abundant porosity of Co/CoS_2/NSCNT, which promotes efficient charge transport and mass diffusion, thereby facilitating the formation of well-developed gas-liquid-solid reaction interfaces [48, 75]. Fig. 6b presents the discharge polarization and power density curves for both ZAB configurations. The Co/CoS_2/NSCNT-based ZAB achieves a peak power density of 163.57 mW cm^{-2} at 0.63 V alongside a maximum current density of 261.53 mA cm^{-2}, significantly surpassing the Pt/C + RuO_2 counterpart (214.21 mA cm^{-2} and 135.73 mW cm^{-2} under identical conditions). Galvanostatic full-discharge measurements conducted at 10 mA cm^{-2} in Fig. 6c reveal that the Co/CoS_2/NSCNT-based ZAB delivers superior specific capacity of 784.08 mAh gZn^{-1}, substantially exceeding the reference system (673 mAh gZn^{-1}) and corresponding to approximately 95.62% of the theoretical capacity (820 mAh gZn^{-1}), indicating highly efficient utilization of the zinc anode throughout the discharge process.

The rate capability of the ZABs was further evaluated by the stepwise increase from 1 to 20 mA cm^{-2} of the discharge current density at 1 h intervals (Fig. 6d). The ZAB with the as-synthesized catalyst achieved excellent discharge voltage stability throughout the entire current range, exhibiting a voltage decay of only 0.15 V by maintaining voltages of 1.36 V and 1.21 V at 1 mA cm^{-2} and 20 mA cm^{-2}, respectively. A discharge voltage of approximately 1.35 V was

re-established after lowering the current density to 1 mA cm^{-2}, suggesting stable charge-discharge reversibility with an insignificant voltage difference (~0.01 V) compared to the initial value. In contrast, the benchmark Pt/C + RuO_2 cathode exhibited a 1.31 V to 0.96 V substantial voltage drop over the identical current range, underscoring the markedly superior rate performance and operational stability of Co/CoS_2/NSCNT. Long-term cycling durability was assessed through galvanostatic charge-discharge measurements at 10 mA cm^{-2} with alternating 5 min charge and discharge steps (Fig. 6e). The Co/CoS_2/NSCNT-based ZAB sustained a charge-discharge profile with a stable narrow voltage gap throughout continuous 100 h operation, while the noble metal-based ZAB showed rapid performance deterioration, failing after approximately 16 h. Quantitatively, the voltaic efficiency of the ZAB based on Co/CoS_2/NSCNT was initially approximately 60% and decreased only slightly to 58% after prolonged cycling, whereas the noble metal-based system, despite initially delivering a higher efficiency of 62%, rapidly declined to 49% within the initial operational period. These results collectively demonstrate that Co/CoS_2/NSCNT enables stable discharge behavior, excellent cycling durability, and high electrochemical reversibility under practical operating conditions, attributed to the encapsulation of Co-based active sites within the NSCNT framework, which effectively inhibits active component agglomeration and alkaline dissolution [17]. A comparative analysis of peak power density and specific capacity against previously reported ZAB air cathodes is presented in Table S5, further confirming the strong competitiveness of Co/CoS_2/NSCNT as a high-performance air cathode material for liquid-state ZAB applications.

Following the outstanding performance demonstrated in liquid-state ZABs, a quasi-solid-state flexible Zn-air battery (FZAB) was constructed to assess the practical applicability of Co/CoS_2/NSCNT in flexible energy storage systems. A polished zinc plate as the anode, Co/CoS_2/NSCNT-coated carbon cloth as the air cathode, and a polyacrylic acid (PAA)-based gel electrolyte were used to assemble the flexible device. The PAA gel was pre-activated by

soaking in 6.0 M KOH containing 0.2 M $Zn(CH_3COO)_2$ to ensure sufficient ionic conductivity. The cell was encapsulated in flexible packaging with an air window to maintain mechanical integrity while enabling efficient oxygen diffusion to the air cathode. A reference FZAB based on Pt/C + RuO_2 (mass ratio 1:1) was prepared under identical conditions for comparison. Fig. 7b shows that the Co/CoS_2/NSCNT-based FZAB exhibits an OCV of 1.43 V, which exceeds the 1.38 V of the Pt/C + RuO_2-based device, indicating a stable electrochemical configuration and effective electrode integration. The discharge polarization curves with power densities of the FZABs are presented in Fig. 7c. The prepared catalyst-based FZAB delivers a peak power density of 95.19 mW cm^{-2}, markedly exceeding the 73.82 mW cm^{-2} achieved by the Pt/C + RuO_2-based FZAB, consistent with the performance trend observed in the liquid-state ZAB and confirming that Co/CoS_2/NSCNT maintains high discharge performance for both rigid and flexible battery configurations. Rate capability was evaluated by the stepwise increase of the discharge current density from (1 to 5 mA cm^{-2}) at fixed time intervals (Fig. 7d). The Co/CoS_2/NSCNT-based FZAB maintained discharge voltages ranging from 1.38 to 1.35 V with only minor voltage decay, and the discharge voltage almost completely recovered to its initial value upon reverting to 1 mA cm^{-2}, demonstrating excellent electrochemical reversibility. By comparison, the Pt/C + RuO_2-based FZAB delivered considerably lower discharge voltages across the same current range. The galvanostatic charge-discharge cycling was conducted for the extended cycling durability evaluation under alternating 5 min charge/discharge intervals at a current density of 10 mA cm^{-2} (Fig. 7e). The Co/CoS_2/NSCNT-based FZAB maintained stable cycling properties for over 25 h without noticeable voltage variation, whereas the reference FZAB exhibited rapid voltage degradation after 6 h. To further evaluate mechanical stability, electrochemical performance was examined under bending conditions at angles of 0°, 60°, and 120°, followed by recovery to its original state (Fig. 7f). The Co/CoS_2/NSCNT-based FZAB exhibited stable charge-discharge behavior throughout the

entire bending process with no discernible performance deterioration, demonstrating excellent mechanical robustness attributed to the flexible carbon cloth substrate, strong catalyst adhesion, and the gel electrolyte system, which together preserve intimate electrode-electrolyte contact during mechanical deformation. Table S6 summarizes the electrolyte type, OCV, and peak power density of Co/CoS_2/NSCNT alongside those of previously reported FZAB air cathodes, further confirming its strong competitiveness as an efficient cathode catalyst for flexible ZAB applications.

To investigate the structural integrity of Co/CoS_2/NSCNT after extended battery cycling, post-cycling analysis was performed. SEM images acquired before and after cycling (Figs. S35a and S35b) confirm that the catalyst preserved its original dodecahedral morphology and CNT network without noticeable structural collapse, demonstrating the excellent mechanical robustness of the carbon framework. XRD analysis of the post-cycling sample (Fig. S36a) revealed no significant shift of the main diffraction peak positions relative to the pristine material, indicating that the overall crystal structure was largely retained. However, slight peak broadening and reduced intensity suggest partial amorphization and surface reconstruction induced by prolonged electrochemical operation [76]. Raman spectroscopy (Fig. S36b) further confirmed the electrochemical durability of the carbon framework, with the characteristic A_{1g} vibrational mode of CoS_2 at 675 cm^{-1} and well-defined D and G bands remaining clearly discernible after cycling. High-resolution XPS Co 2p analysis (Fig. S36c) showed that the binding energy positions and relative peak intensities were well-maintained after cycling, confirming the absence of severe chemical degradation. EIS measurements conducted before and after the stability test over a frequency range of 0.1 Hz to 100 kHz (Fig. S37) revealed that the internal resistance of Co/CoS_2/NSCNT electrode exhibited only a negligible increase from 8.11 to 8.62 Ω, confirming the exceptional structural integrity of the catalyst framework throughout prolonged cycling. In sharp contrast, the $Pt/C + RuO_2$ benchmark system exhibited

a substantially larger elevation from 9.48 to 12.11 Ω, primarily attributed to structural degradation of the noble metal particles and increased interfacial charge transfer resistance, consistent with the severe voltage deterioration observed in the galvanostatic charge-discharge profiles. These comprehensive post-cycling characterization results collectively confirm that Co/CoS_2/NSCNT possesses outstanding structural and chemical integrity, establishing its suitability as a highly durable bifunctional electrocatalyst for practical ZAB applications.

In summary, the outstanding electrocatalytic activity of Co/CoS_2/NSCNT demonstrated across all three device configurations, namely AEMFC, liquid-state ZAB, and flexible ZAB, originates from the synergistic integration of its structural architecture and interfacial chemistry. First, the hierarchical porous framework generated through Zn volatilization and NaCl-assisted synthesis expands the electrochemically active surface area and accelerates mass transfer by creating internal mesopores through Zn evaporation while the molten NaCl template preserves the rhombic dodecahedral geometry [23, 26, 28]. Second, the in-situ grown NSCNTs establish a robust three-dimensional conductive network that accelerates charge transfer kinetics while physically encapsulating the Co-based active cores to ensure structural integrity and long-term durability [16, 17]. Third, the synergistic combination of N, S dual-heteroatom doping and Co/CoS_2 Mott-Schottky heterojunction formation optimizes the local electronic environment through enhanced surface polarity and built-in electric field generation, effectively lowering the energy barriers for oxygen intermediate ad/desorption [13, 18]. The integration of these rational design strategies positions Co/CoS_2/NSCNT as a high-performance and durable bifunctional electrocatalyst platform for next-generation energy conversion and storage technologies.

Conclusion

In this study, a high-performance bifunctional electrocatalyst consisting of a Co/CoS_2 Mott-

Schottky heterojunction encapsulated within N, S co-doped carbon nanotubes (Co/CoS_2/NSCNT) was successfully synthesized via a facile NaCl-assisted pyrolysis strategy. The synergistic combination of Zn volatilization and molten salt templating effectively preserved the rhombic dodecahedral morphology while generating a hierarchical mesoporous framework with an enlarged specific surface area of 255.68 $m^2 g^{-1}$, facilitating efficient mass transport and enhanced reactant accessibility. The in-situ growth of conductive CNT networks on the nanoparticle surfaces established a robust three-dimensional electron transport highway, contributing to rapid charge transfer kinetics and long-term electrochemical stability during prolonged operation. Furthermore, N, S dual-heteroatom doping combined with electronic redistribution at the Co/CoS_2 Mott-Schottky heterointerface synergistically lowered the activation energy barriers for oxygen intermediates, enabling exceptional bifunctional electrocatalytic performance. Specifically, Co/CoS_2/NSCNT achieved a superior ORR half-wave potential of 874 mV vs. RHE and a low OER overpotential of 334 mV at 10 mA cm^{-2}, surpassing commercial Pt/C and RuO_2 benchmarks as well as many previously reported non-precious metal electrocatalysts. The AEMFC employing Co/CoS_2/NSCNT as an air cathode catalyst achieved a peak power density of 199.15 mW cm^{-2}, surpassing that of the commercial Pt/C benchmark. When employed as the air cathode in a liquid-state ZAB, the device delivered a high specific capacity of 784.08 mAh gZn^{-1} and a peak power density of 163.57 mW cm^{-2} with remarkable long-term cycling performance over 100 h. Additionally, the quasi-solid-state flexible ZAB demonstrated excellent mechanical robustness and a peak power density of 95.19 mW cm^{-2}, confirming the suitability of Co/CoS_2/NSCNT for flexible and wearable energy storage devices. The obtained results underscore the strong advantages of rationally integrating hierarchical porosity, conductive carbon networks, and heterointerface engineering, while providing meaningful design guidelines for the development of sustainable, noble-metal-free bifunctional electrocatalysts for next-generation energy conversion and storage technologies.

CRediT authorship contribution statement

Hyeongseok Seo: Conceptualization, Formal analysis, Investigation, Writing - original draft. **Hoyeon Kang**: Data curation, Investigation. **Sejin Kim**: Data curation, Formal analysis. **Sang Eun Shim:** Writing – review & editing. **Sung-Hyeon Baeck**: Funding acquisition, Project administration, Resources, Supervision, Writing - review & editing.

Declaration of Competing Interest

The authors declare that they have no known competing financial interests or personal relationships that could have appeared to influence the work reported in this paper.

Data Availability

On request

Funding

This work was supported by the Institute of Information & Communications Technology Planning & Evaluation(IITP)-Innovative Human Resource Development for Local Intellectualization program grant funded by the Korea government(MSIT)(IITP-2025-RS-2023-00259678), and by Korea Institute for Advancement of Technology(KIAT) grant funded by the Korea Government(MOTIE) (RS-2025-02073015, HRD Program for Industrial Innovation).

References

1. Hao H, Wang J, Huang Q, et al (2026) Deciphering the bidirectional reconstructions

and lattice oxygen activation for high-performance bifunctional oxygen electrocatalysis in Zn-air batteries. Appl Catal B Environ 393:126763. https://doi.org/10.1016/j.apcatb.2026.126763

2. Peng J, Li Z, Liu W, et al (2026) Clusters induced electron redistribution of single-atom Co sites in freestanding nanofiber electrodes for efficient Zn-Air batteries. Appl Catal B Environ 399:127080. https://doi.org/10.1016/j.apcatb.2026.127080
3. Xu M, Wang T, Jiang T, et al (2026) Boosting AEMFC performance via tailored interactions between poly(fluorenylene alkylene) ionomer and Pt/C catalysts. J Memb Sci 738:124911. https://doi.org/10.1016/j.memsci.2025.124911
4. Ma N, Liu H, Yu L, et al (2026) Mechanistic Understanding of Curvature Effects on ORR/OER Activity in Single-Atom Catalysts From Atomic-Scale Perspective. Small. https://doi.org/10.1002/smll.202513102
5. Xie Y, Zheng T, Wang J, Ding W (2026) A Critical Challenge for Anion Exchange Membrane Fuel Cells (AEMFCs): Insufficient Stability of Non-Precious Cathode Catalyst. Small 2:30–35. https://doi.org/10.1002/smll.73564
6. Zhao Y, Adiyeri Saseendran DP, Huang C, et al (2023) Oxygen Evolution/Reduction Reaction Catalysts: From In Situ Monitoring and Reaction Mechanisms to Rational Design. Chem Rev 123:6257–6358. https://doi.org/10.1021/acs.chemrev.2c00515
7. Pradhan AK, Halder S, Palani SG, Chakraborty C (2025) Hierarchical graphitic carbon nitride-polypyrrole on metal-organic framework-derived carbon nanorod: Metal-Free electrocatalyst for solid-state flexible zinc-air batteries. J Power Sources 659:238425. https://doi.org/10.1016/j.jpowsour.2025.238425
8. Seong H, Min K, Lee G, et al (2025) Development of an efficient bifunctional electrocatalyst based on Co/CoSe2 nanoparticles embedded in N, Se co-doped carbon for AEMFC and rechargeable Zn-air battery. Appl Catal B Environ 362:.

https://doi.org/10.1016/j.apcatb.2024.124725

9. Pramanik A, Sengupta S, Saju SK, et al (2024) Ternary Metal Sulfides as Electrode Materials for Na/K-Ion Batteries and Electrochemical Supercapacitor: Advances/Challenges and Prospects. Adv Energy Mater 14:. https://doi.org/10.1002/aenm.202401657
10. Jiang J, Sun R, Huang X, et al (2023) In-situ derived Mo-doped NiCoP and MXene to form Mott-Schottky heterojunction with tunable surface electron density to promote overall water splitting. Compos Part B Eng 263:110834. https://doi.org/10.1016/j.compositesb.2023.110834
11. Xu X, Liao H, Huang L, et al (2024) Surface reconstruction and directed electron transport in NiSe2/MoSe2 Mott-Schottky heterojunction catalysts promote urea-assisted water splitting. Appl Catal B Environ 341:123312. https://doi.org/10.1016/j.apcatb.2023.123312
12. Xue J, Bao J (2021) Interfacial charge transfer of heterojunction photocatalysts: Characterization and calculation. Surfaces and Interfaces 25:101265. https://doi.org/10.1016/j.surfin.2021.101265
13. Xin R, Zhao H, Liu Y, et al (2025) Homologous Mott–Schottky Electrocatalysts Enable Record Cycling Stability in Zn-Air Battery and Water Splitting. Adv Funct Mater 24205:1–15. https://doi.org/10.1002/adfm.202524205
14. Lang X, Huang J, Zhang M, et al (2025) A scalable synthesis strategy for Mott-Schottky heterojunction with Ni3S2 as a self-supporting template for boosting OER/MOR. J Alloys Compd 1026:180478. https://doi.org/10.1016/j.jallcom.2025.180478
15. Chen H, Lv E, Qin M, et al (2025) Mott-Schottky heterojunction design in Cu/Fe2N@NC catalyst with interfacial electron redistribution for enhanced oxygen

reduction reaction in zinc-air batteries. J Alloys Compd 1032:181134. https://doi.org/10.1016/j.jallcom.2025.181134

16. Ge Z, Wang X, Lei X, et al (2024) Carbon Nanotubes as Controllable Electric-Field-Induced Bipolar Electrodes for Efficient Water Purification. Environ Sci Technol 58:11843–11854. https://doi.org/10.1021/acs.est.4c03218
17. Geng B, Chen R, Song Q, Li G (2026) Exposed and encapsulated NiMo alloy nanoparticles in a N-doped carbon nanotube array for synergistic catalysis toward efficient industrial water splitting. Chem Eng J 531:173955. https://doi.org/10.1016/j.cej.2026.173955
18. Zhi S, Dai Q, Wang H, et al (2025) Heteroatom-DopedCarbon Materials for MultifunctionalNoncatalytic Applications. ACS Nano 19:29860–29897. https://doi.org/10.1021/acsnano.5c04478
19. Li G, Tang Y, Fu T, et al (2022) S, N co-doped carbon nanotubes coupled with CoFe nanoparticles as an efficient bifunctional ORR/OER electrocatalyst for rechargeable Zn-air batteries. Chem Eng J 429:132174. https://doi.org/10.1016/j.cej.2021.132174
20. Kim IT, Kim SH, Ha JS, et al (2023) Oxygen deficient yolk-shell structured Co3O4 microspheres as an oxygen evolution reaction electrocatalyst for anion exchange membrane water electrolyzers. J Mater Chem A 11:16578–16585. https://doi.org/10.1039/d3ta02710d
21. Sun L, Lv H, Feng J, et al (2022) Noble-Metal-Based Hollow Mesoporous Nanoparticles: Synthesis Strategies and Applications. Adv Mater 34:. https://doi.org/10.1002/adma.202201954
22. Muhammad S, Wang L, Gao M, et al (2026) Fe-Ce interaction-driven active site modulation in a porous MOF for oxygen evolution reaction. Fuel 405:. https://doi.org/10.1016/j.fuel.2025.136782

23. Qian X, Meng X, Sun J, et al (2019) Salt-Assisted Synthesis of 3D Porous g-C3N4 as a Bifunctional Photo- and Electrocatalyst. ACS Appl Mater Interfaces 11:27226–27232. https://doi.org/10.1021/acsami.9b08651

24. Zhang F, Lei Y, Li G, et al (2025) FeCo Bimetallic ZIF Derivatives Decorated with CoFe-LDH to Promote Bifunctional Oxygen Electrocatalysis Activation. ChemSusChem 18:1–9. https://doi.org/10.1002/cssc.202401556

25. Chen A, Cheng M, Huang D, et al (2024) Versatile metal-free carbon materials from ZIF-8: Insights into construction strategies, properties, applications and structure-activity relationships. Renew Sustain Energy Rev 199:. https://doi.org/10.1016/j.rser.2024.114520

26. Wang Q, Yang Y, Sun F, et al (2021) Molten NaCl-Assisted Synthesis of Porous Fe-N-C Electrocatalysts with a High Density of Catalytically Accessible FeN4 Active Sites and Outstanding Oxygen Reduction Reaction Performance. Adv Energy Mater 11:1–9. https://doi.org/10.1002/aenm.202100219

27. Zhang L, Yang Y, Zhong Z, et al (2025) Molten NaCl-assisted preparation of Fe and Co co-modified N-doped porous carbon derived from ZIFs as ORR/OER bifunctional catalyst for zinc-air batteries. Electrochim Acta 544:147521. https://doi.org/10.1016/j.electacta.2025.147521

28. Chiang YC, Chin WT (2022) Preparation of Zeolitic Imidazolate Framework-8-Based Nanofiber Composites for Carbon Dioxide Adsorption. Nanomaterials 12:. https://doi.org/10.3390/nano12091492

29. Miyake Y, Seo G, Matsuhashi K, et al (2021) Synthesis of carbon nitride oligomer as a precursor of melon with improved fluorescence quantum yield. Mater Adv 2:6083–6093. https://doi.org/10.1039/d1ma00579k

30. Zhang D, Ding R, Tang Y, et al (2022) Stable Co/N-Doped Carbon Nanotubes as

Catalysts for Oxygen Reduction. ACS Appl Nano Mater 5:10026–10035. https://doi.org/10.1021/acsanm.2c02453

31. Gueon D, Ju MY, Moon JH (2020) Complete encapsulation of sulfur through interfacial energy control of sulfur solutions for high-performance Li−S batteries. Proc Natl Acad Sci U S A 117:12686–12692. https://doi.org/10.1073/pnas.2000128117
32. Kaur G, Rai RK, Tyagi D, et al (2016) Room-temperature synthesis of bimetallic Co-Zn based zeolitic imidazolate frameworks in water for enhanced CO2 and H2 uptakes. J Mater Chem A 4:14932–14938. https://doi.org/10.1039/c6ta04342a
33. Cai J, Chen Y, Song H, et al (2020) MOF derived C/Co@C with a “one-way-valve”-like graphitic carbon layer for selective semi-hydrogenation of aromatic alkynes. Carbon N Y 160:64–70. https://doi.org/10.1016/j.carbon.2020.01.006
34. Oh YJ, Park JH, Park JS, et al (2022) Fast-chargeable N-doped multi-oriented graphitic carbon as a Li-intercalation compound. Energy Storage Mater 44:416–424. https://doi.org/10.1016/j.ensm.2021.10.036
35. Nguyen T Van, Son LT, Thao PM, et al (2020) One-step solvothermal synthesis of mixed nickel–cobalt sulfides as high-performance supercapacitor electrode materials. J Alloys Compd 831:1–10. https://doi.org/10.1016/j.jallcom.2020.154921
36. Reinsch BC, Levard C, Li Z, et al (2012) Sulfidation of silver nanoparticles decreases Escherichia coli growth inhibition. Environ Sci Technol 46:6992–7000. https://doi.org/10.1021/es203732x
37. Liu X, Choi J, Xu Z, et al (2024) Raman Spectroscopy Measurements Support Disorder-Driven Capacitance in Nanoporous Carbons. J Am Chem Soc 146:30748–30752. https://doi.org/10.1021/jacs.4c10214
38. Zhang H, Nie B, Hu F, et al (2025) Thermal properties and in situ Raman structural evolution of different rank coals during argon heating. Therm Sci Eng Prog 64:103812.

https://doi.org/10.1016/j.tsep.2025.103812

39. Zhang W, Guo X, Li C, et al (2023) Ultralong nitrogen/sulfur Co-doped carbon nano-hollow-sphere chains with encapsulated cobalt nanoparticles for highly efficient oxygen electrocatalysis. Carbon Energy 5:1–16. https://doi.org/10.1002/cey2.317

40. Xu J, Ye P, Cheng Y, et al (2023) Metal–Organic Framework–Based CoS2 Nitrogen-Doped Carbon for High-Performance Lithium Storage. Energy Technol 11:2–9. https://doi.org/10.1002/ente.202201452

41. Kim GM, Lim WG, Kang D, et al (2020) Transformation of carbon dioxide into carbon nanotubes for enhanced ion transport and energy storage. Nanoscale 12:7822–7833. https://doi.org/10.1039/c9nr10552b

42. Na R, Min K, Kim H, et al (2023) Boosting electrocatalytic activity with the formation of abundant heterointerfaces and N, S dual-doped carbon nanotube for rechargeable Zn-air battery. J Energy Chem 84:140–152. https://doi.org/10.1016/j.jechem.2023.05.040

43. Zhou M, Chen B, Zhang N, et al (2023) Intrinsic Carbon Defects in Nitrogen and Sulfur Doped Porous Carbon Nanotubes Accelerate Oxygen Reduction and Sulfur Reduction for Electrochemical Energy Conversion and Storage. ACS Appl Nano Mater 6:15147–15158. https://doi.org/10.1021/acsanm.3c02803

44. Yu S, Liu D, Wang C, et al (2024) Nanosheet-assembled transition metal sulfides nanoflowers derived from CoMo-MOF for efficient oxygen evolution reaction. J Colloid Interface Sci 653:1464–1477. https://doi.org/10.1016/j.jcis.2023.10.006

45. He X, Zhu Q, Li J, Lin L (2023) Defect-Rich MoS2/CoS2 Supported on In Situ Formed Graphene Layers for Efficient Overall Water Splitting. Catal Letters 153:3805–3816. https://doi.org/10.1007/s10562-023-04275-5

46. Zheng M, Zhao J, Wu W, et al (2024) Co/CoS2 Heterojunction Embedded in N, S-

Doped Hollow Nanocage for Enhanced Polysulfides Conversion in High-Performance Lithium–Sulfur Batteries. Small 20:1–13. https://doi.org/10.1002/smll.202303192

47. Shamsipur M, Safavi A, Mohammadpour Z, Ahmadi R (2016) Highly selective aggregation assay for visual detection of mercury ion based on competitive binding of sulfur-doped carbon nanodots to gold nanoparticles and mercury ions. Microchim Acta 183:2327–2335. https://doi.org/10.1007/s00604-016-1870-z

48. Shang W, Yu W, Ma Y, et al (2021) Constructing the Triple-Phase Boundaries of Integrated Air Electrodes for High-Performance Zn–Air Batteries. Adv Mater Interfaces 8:1–9. https://doi.org/10.1002/admi.202101256

49. Yao W, Hu A, Ding J, et al (2023) Hierarchically Ordered Macro–Mesoporous Electrocatalyst with Hydrophilic Surface for Efficient Oxygen Reduction Reaction. Adv Mater 35:1–8. https://doi.org/10.1002/adma.202301894

50. Son Y, Min K, Cheong S, et al (2024) Innovative Air Cathode with Ni-Doped Cobalt Sulfide in Highly Ordered Macroporous Carbon Matrix for Rechargeable Zn–Air Battery. Adv Sci 11:1–14. https://doi.org/10.1002/advs.202407915

51. Gao B, Tan M, Xi W, et al (2022) Co-embedded carbon nanotubes modified N-doped carbon derived from poly(Schiff base) and zeolitic imidazole frameworks as efficient oxygen electrocatalyst towards rechargeable Zn-air battery. J Power Sources 527:. https://doi.org/10.1016/j.jpowsour.2022.231205

52. Kim K, Kang T, Kim M, Kim J (2021) Exploring the intrinsic active sites and multi oxygen evolution reaction step via unique hollow structures of nitrogen and sulfur co-doped amorphous cobalt and nickel oxides. Chem Eng J 426:130820. https://doi.org/10.1016/j.cej.2021.130820

53. Han K, Dai P, Yang Y, Wu M (2022) FeS2/CoS2 nanoparticles supported on N, S co-doped carbon nanotubes as advanced bifunctional electrocatalysts for rechargeable

zinc-air batteries. Mater Res Bull 154:111942. https://doi.org/10.1016/j.materresbull.2022.111942

54. Wang X, Zhan G, Wang Y, et al (2022) Engineering core–shell Co9S8/Co nanoparticles on reduced graphene oxide: Efficient bifunctional Mott–Schottky electrocatalysts in neutral rechargeable Zn–Air batteries. J Energy Chem 68:113–123. https://doi.org/10.1016/j.jechem.2021.09.014

55. Wang X, Sun R, Xie G, et al (2025) Multi-heteroatom co-doped sodium alginate/sodium lignosulfonate hierarchical porous carbon aerogels for high-performance supercapacitors. Mater Today Commun 48:113563. https://doi.org/10.1016/j.mtcomm.2025.113563

56. Liu Q, Liu X, Xie Y, et al (2020) N-Doped carbon coating enhances the bifunctional oxygen reaction activity of CoFe nanoparticles for a highly stable Zn-Air battery. J Mater Chem A 8:21189–21198. https://doi.org/10.1039/d0ta08114k

57. Xing G, Zhang G, Wang B, et al (2023) Strengthening oxygen reduction activity based on the cooperation of pyridinic-N and graphitic-N for atomically dispersed Fe sites. J Mater Chem A 11:9493–9503. https://doi.org/10.1039/d3ta00899a

58. Liu L, Hussain MZ, Lei D, et al (2025) Cobalt-Based Catalyst Integration Into a Hierarchically Ordered Macro-Meso-microporous Carbon Cathode for High-performance Aqueous Zn-Sulfur Batteries. Adv Sci 12:. https://doi.org/10.1002/advs.202509945

59. Lu Y, Li Z, Feng J, et al (2025) Synergistic molecular and heterojunction engineering of sulfonyl-functionalized perylene diimide polymers for enhanced visible-light photocatalysis. New J Chem 2249–2258. https://doi.org/10.1039/d5nj04534g

60. Elmouwahidi A, Vivo-Vilches JF, Pérez-Cadenas AF, et al (2016) Free metal oxygen-reduction electro-catalysts obtained from biomass residue of the olive oil industry.

Chem Eng J 306:1109–1115. https://doi.org/10.1016/j.cej.2016.08.042

61. Varodi C, Pogăcean F, Cioriță A, et al (2021) Nitrogen and sulfur co-doped graphene as efficient electrode material for l-cysteine detection. Chemosensors 9:1–16. https://doi.org/10.3390/chemosensors9060146

62. Qin Y, Zhang C, Wang Y, et al (2025) Electrostatic Attraction-Driven Assembly of Non-Noble Metallo-Supramolecular Polymers With Single-Walled Carbon Nanotubes for Boosting Photocatalytic Hydrogen Evolution. Carbon Energy 7:1–10. https://doi.org/10.1002/cey2.70003

63. Chen Y, Huang Q, Zhao R, et al (2024) Tuning Work Function of Fe2N@C Nanosheets by Co Doping for Enhanced Lithium Storage. Small 2405608:1–8. https://doi.org/10.1002/smll.202405608

64. Pei L, Zhong J, Li T, et al (2020) CoS2@N-doped carbon core-shell nanorod array grown on Ni foam for enhanced electrocatalytic water oxidation. J Mater Chem A 8:6795–6803. https://doi.org/10.1039/d0ta00777c

65. Jin H, Zhang Y, Cao Z, et al (2025) Atomically Dispersed Sn on Core-Shell MoS2 Nanoreactors as Mott-Schottky Phase Junctions for Efficient Electrocatalytic Hydrogen Evolution. Adv Mater 37:. https://doi.org/10.1002/adma.202502977

66. Jiang P, Ge B, Cheng C, Huang C (2025) Balancing electrophilic and nucleophilic dual sites to construct efficient Mott–Schottky oxygen electrocatalysts. Chem Eng Sci 306:121249. https://doi.org/10.1016/j.ces.2025.121249

67. Tong Y, Liu W, Li C, et al (2022) A metal/semiconductor contact induced Mott-Schottky junction for enhancing the electrocatalytic activity of water-splitting catalysts. Sustain Energy Fuels 7:12–30. https://doi.org/10.1039/d2se01355j

68. Meng Y, Xiang C, Zhang W, et al (2025) Heteroatom-Engineering Promoted Co9S8 Bi-functional Electrocatalyst for Hydrazine-Assisted Hydrogen Production at

Industrial Current Density. Adv Funct Mater 1–13. https://doi.org/10.1002/adfm.202524807

69. Yi M, Chu L, Lv S, et al (2025) Synergistic engineering of heterointerfaces and defects in N, P-codoped carbon-encapsulated MnSe/NiSe2 heterostructure for efficient alkaline hydrogen evolution and high-performance flexible supercapacitors. Energy Storage Mater 83:. https://doi.org/10.1016/j.ensm.2025.104725

70. Cheong S, Shin J, Kang S, et al (2026) Vanadium-doped cobalt selenide nanoparticles embedded in mesoporous hollow carbon spheres as highly efficient bifunctional electrocatalyst for rechargeable Zn-air batteries. Carbon N Y 250:121318. https://doi.org/10.1016/j.carbon.2026.121318

71. Yang R, Wang Q, Xi L, et al (2025) Co/C hollow porous nanocomposite derived from Zn-MOF-on-Co-MOF heterostructures based on volatilization of Zinc enable robust low frequency electromagnetic wave absorption. Mater Today Commun 49:113715. https://doi.org/10.1016/j.mtcomm.2025.113715

72. Pierlot AP, Woodhead AL, Church JS (2014) Thermal annealing effects on multi-walled carbon nanotube yarns probed by Raman spectroscopy. Spectrochim Acta - Part A Mol Biomol Spectrosc 117:598–603. https://doi.org/10.1016/j.saa.2013.09.050

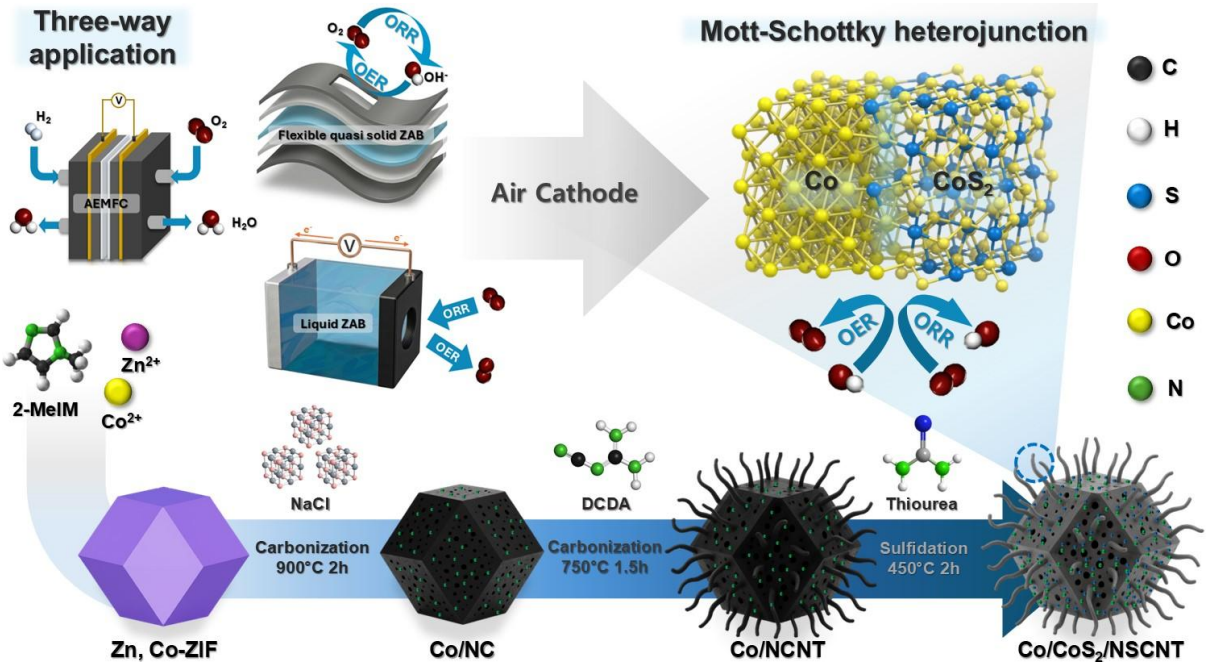
73. Gao X, Lu X, Zhong J, et al (2025) High-performance hybrid supercapacitors based on cobalt sulfide and iron sulfide nanoparticles supported by hollow nitrogen–sulfur co-doped carbon spheres. Inorg Chem Front 12:8595–8603. https://doi.org/10.1039/d5qi01452b

74. Min S, Min K, Lee G, et al (2024) Enhancing electrocatalytic performance for rechargeable Zn-air battery through interface engineering and dual-doping strategy. J Energy Storage 86:111298. https://doi.org/10.1016/j.est.2024.111298

75. Lee H, Lee B, Shin J, et al (2026) Heterostructured cobalt sulfides in N, S dual-doped

hollow carbon spheres for high-performance rechargeable liquid and flexible Zn-air batteries. J Energy Storage 154:121213. https://doi.org/10.1016/j.est.2026.121213

76. Cha Y, Jang H, Noh D, et al (2025) Precisely controllable microwave-driven reconstruction of Ni-Co-Fe trimetallic needle structures on nitrogen-doped carbon as bifunctional oxygen catalysts for Zn–air batteries. Adv Compos Hybrid Mater 8:. https://doi.org/10.1007/s42114-025-01421-y



Scheme 1. Schematic illustration of NaCl-assisted Co/CoS_2/NSCNT electrocatalyst synthesized by heteroatom doping and interface engineering.

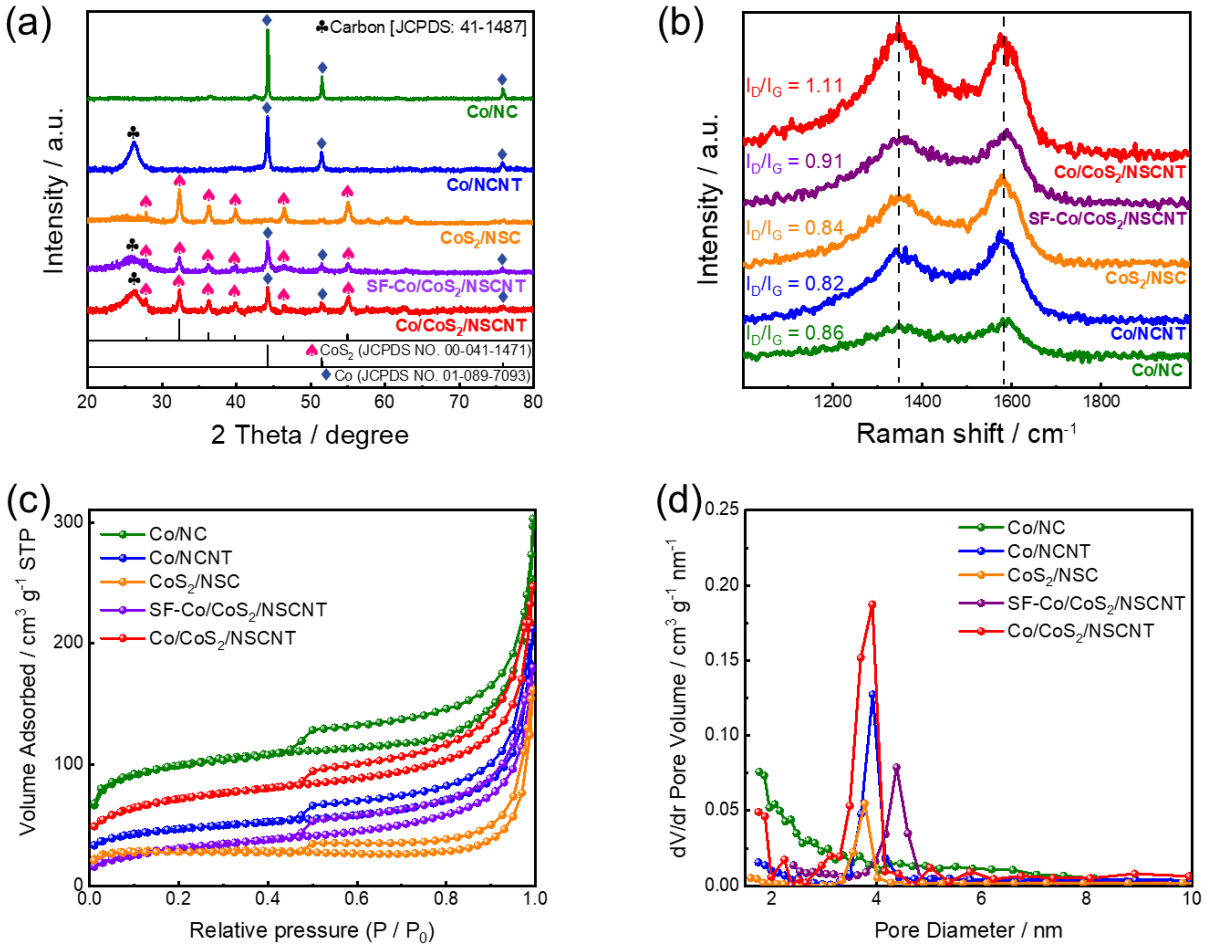


Fig. 1. (a) X-ray diffraction (XRD) patterns, (b) Raman spectra, (c) N_2 adsorption-desorption isotherm curves, and (d) corresponding pore size distribution of Co/NC, Co/NCNT, CoS_2/NSC, SF-Co/CoS_2/NSCNT, and Co/CoS_2/NSCNT.

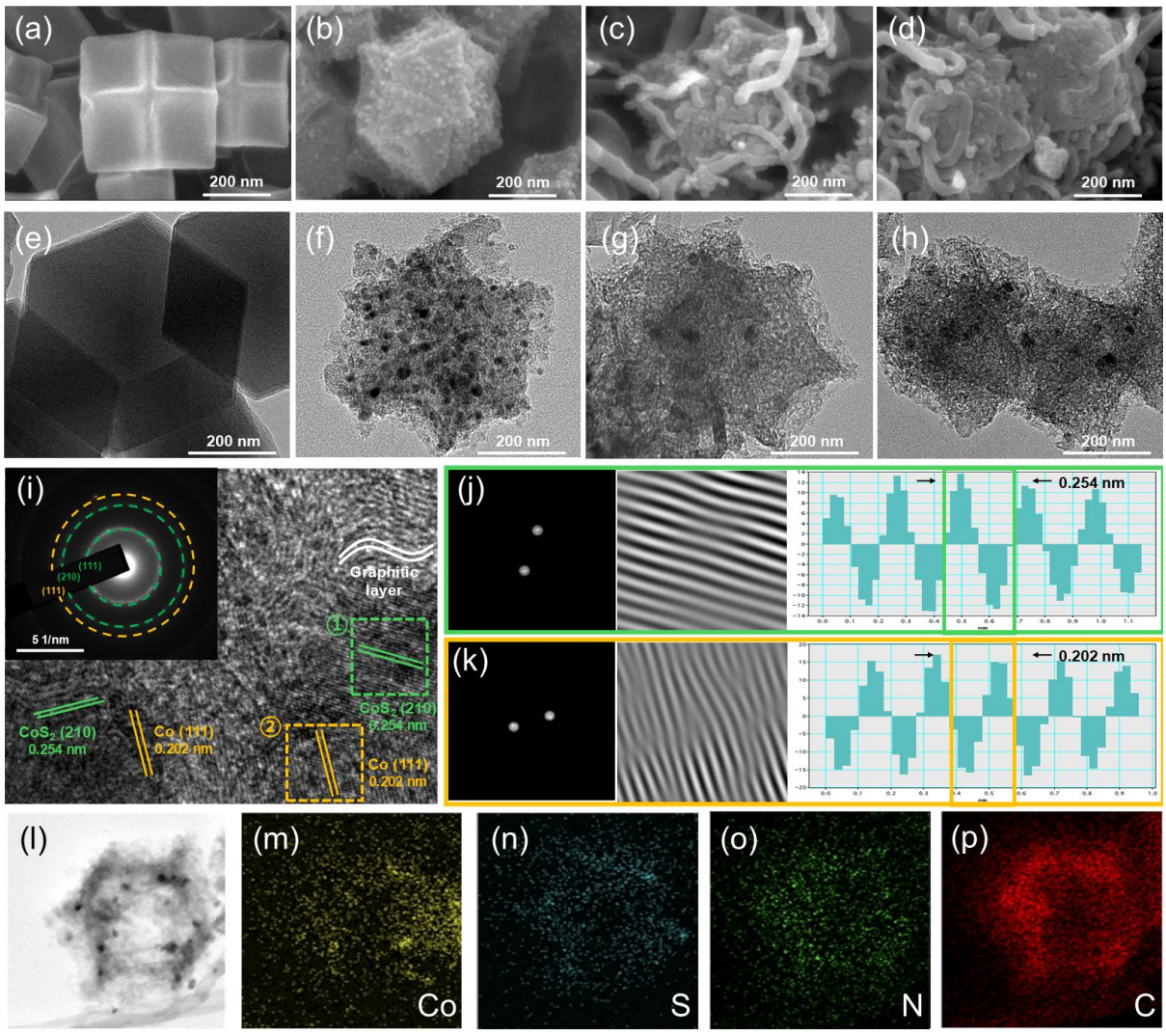


Fig. 2. Scanning electron microscopy (SEM) and transmission electron microscopy (TEM) images of (a and e) Zn, Co-ZIF, (b and f) Co/NC, (c and g) Co/NCNT, and (d and h) Co/CoS_2/NSCNT. (i) Selected area electron diffraction (SAED) pattern and High-resolution

TEM (HRTEM) image of Co/CoS_2/NSCNT and corresponding FFT and IFFT images of (j) CoS_2 and (k) Co species. (l-p) EDS elemental mapping images of the Co/CoS_2/NSCNT.

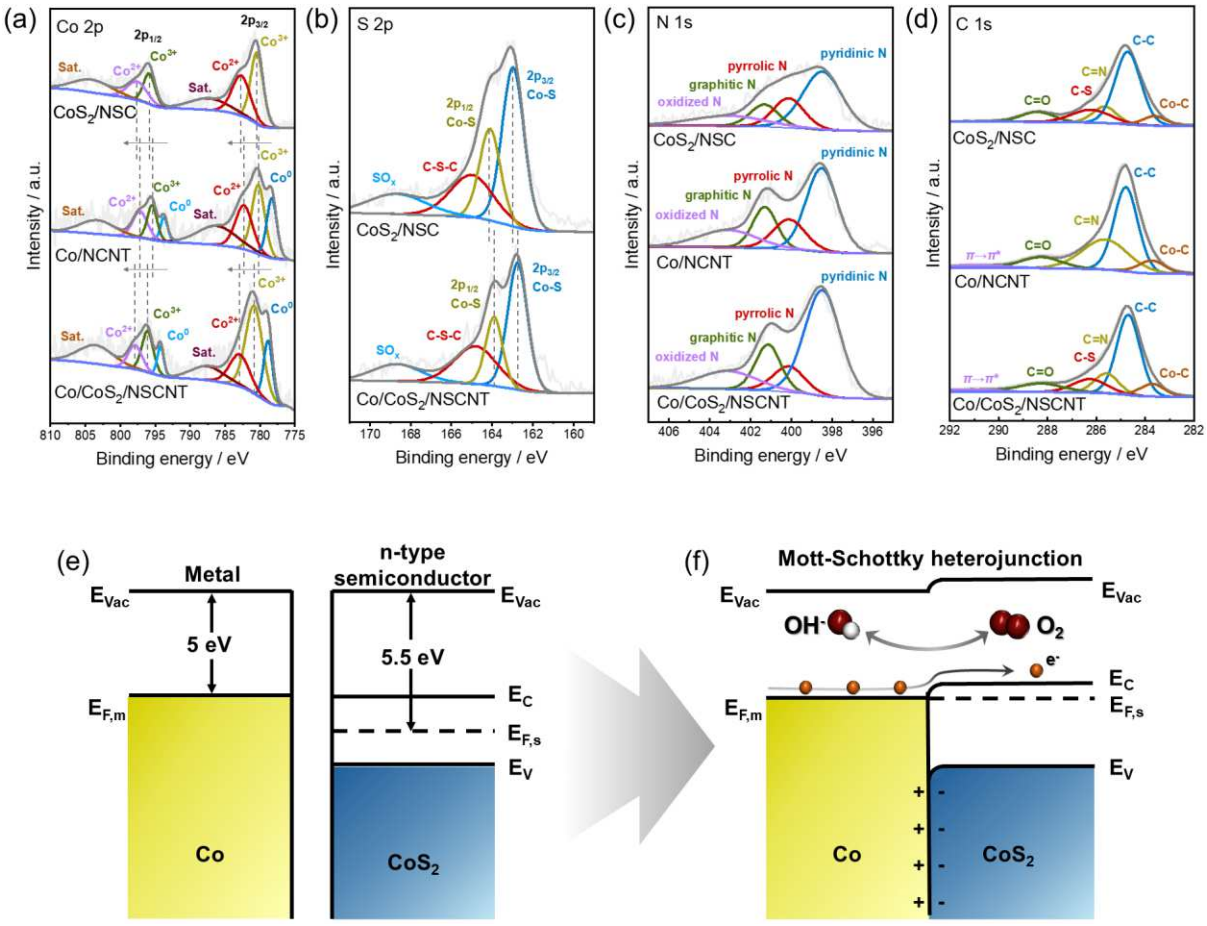


Fig. 3. XPS spectra of (a) Co 2p, (b) S 2p, (c) N 1s, and (d) C 1s for CoS_2/NSC, Co/NCNT, and Co/CoS_2/NSCNT. Energy band modification for metallic Co and n-type CoS_2 semiconductor (e) before and (f) after the Mott-Schottky junction.

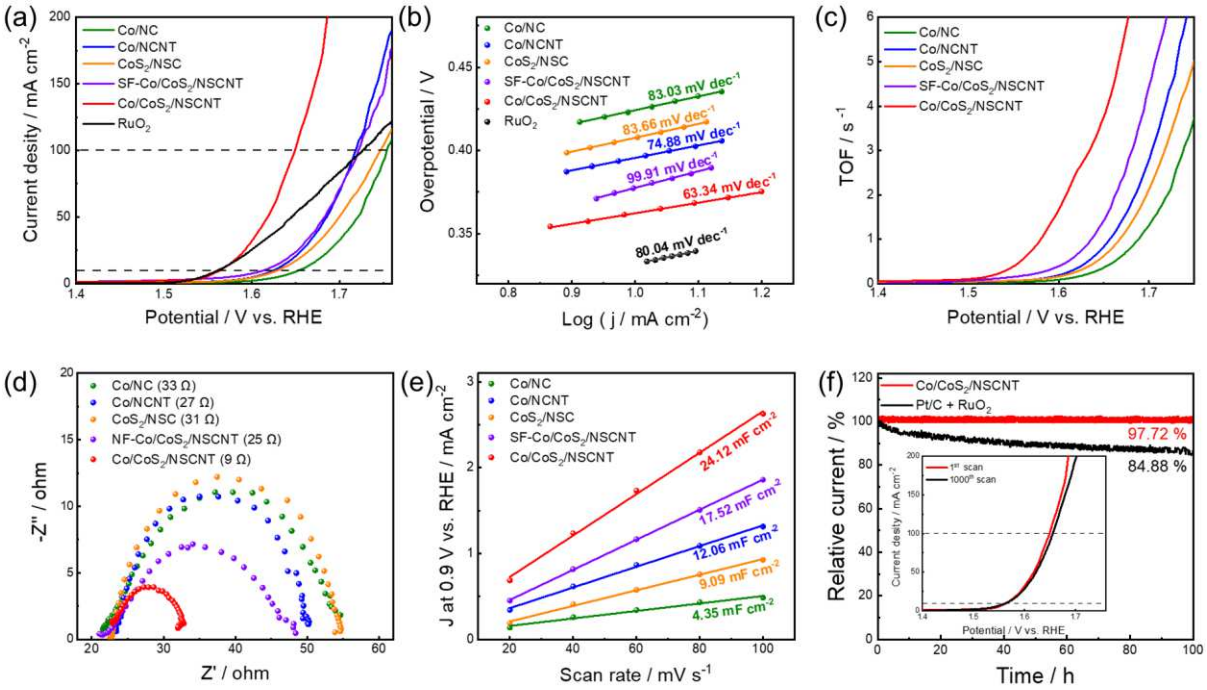


Fig. 4. Electrochemical characterization of prepared electrocatalysts for OER. (a) LSV polarization curves measured in N_2-saturated 0.1 M KOH solutions by a scan rate of 5 mV s^{-1} and (b) corresponding Tafel plots of prepared electrocatalysts. (c) TOF curves obtained by conversion of corresponding polarization curves. (d) Nyquist plots obtained from EIS measurements. (e) Linear plots of capacitive current densities with respect to different scan rates. (f) CA response of $Co/CoS_2/NSCNT$; the inset shows the polarization curves before and after ADT measurement.

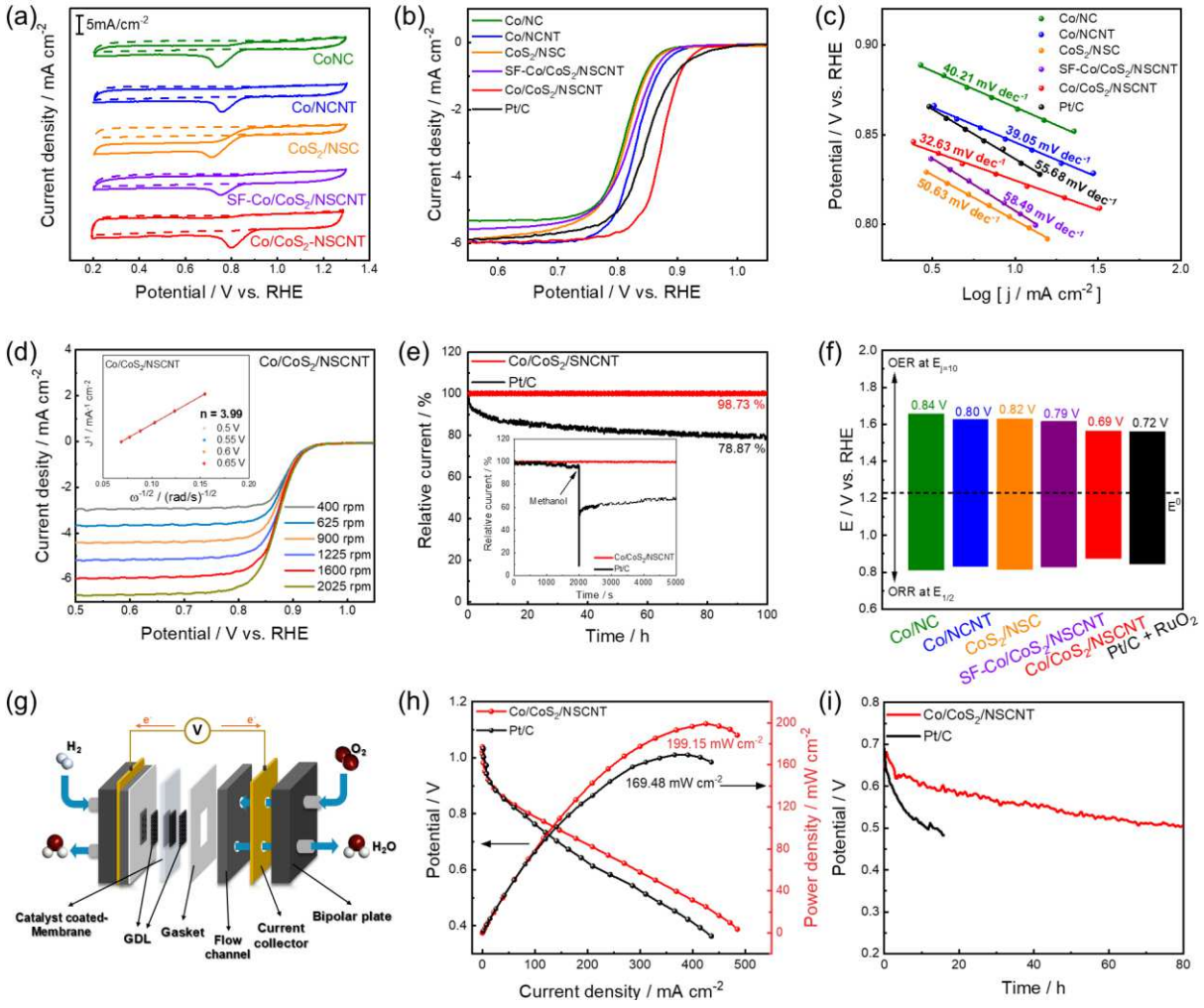


Fig. 5. Electrochemical characterization of prepared electrocatalysts for ORR. (a) CV curves measured at a potential range of 0.2–1.3 V vs. RHE in N_2-saturated (dashed line) and O_2-saturated (solid line) 0.1 M KOH solutions. (b) LSV polarization curves measured in O_2-saturated 0.1 M KOH solutions by 1600 rpm and a scan rate of 5 mV s^{-1} and (c) corresponding Tafel plots of prepared electrocatalysts. (d) Rotating disk voltammograms of $Co/CoS_2/NSCNT$ at rotation rates of 400–2025 rpm. The inset of (d) represents the Koutecky–Levich plots at different potentials (0.5–0.65 V vs. RHE). (e) Long-term chronoamperometric (CA) responses of $Co/CoS_2/NSCNT$ and Pt/C. The inset of (e) represents the methanol tolerance test conducted by adding methanol to the electrolyte at 2000s during CA measurement. (f) Summary of calculated potential gaps ($\Delta E = E_{j=10} - E_{1/2}$) for prepared samples and commercial $Pt/C + RuO_2$ catalyst. (g) Schematic illustration of the anion exchange membrane fuel cell (AEMFC). (h)

Single cell polarization profiles with the corresponding power density curves and (i) Long-term chronopotentiometry (CP) results of Co/CoS_2/NSCNT and Pt/C-based AEMFC.

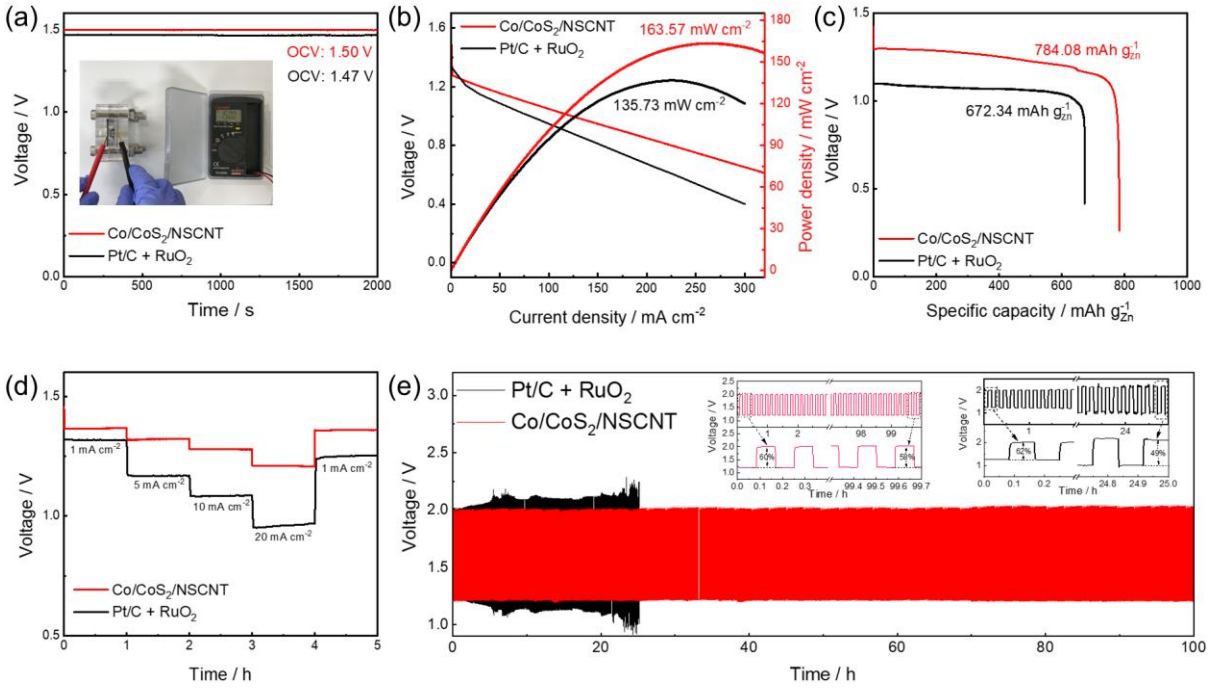


Fig. 6. Electrochemical performance of aqueous rechargeable ZABs assembled using $Co/CoS_2/NSCNT$ and $Pt/C+RuO_2$ electrocatalysts as air cathode. (a) OCV profiles; the inset shows digital photograph of OCV value for $Co/CoS_2/NSCNT$-based flexible ZAB, (b) discharge polarization curves and the corresponding power density curves, (c) galvanostatic full-discharge curves with current density of 10 mA cm^{-2}, and (d) constant discharge voltages at various current densities of $Co/CoS_2/NSCNT$-(red) and $Pt/C+RuO_2$-(black) based ZABs. (e) Long-term galvanostatic charge/discharge cycling performance at a pulse current density of 10 mA cm^{-2} with 5 min intervals.

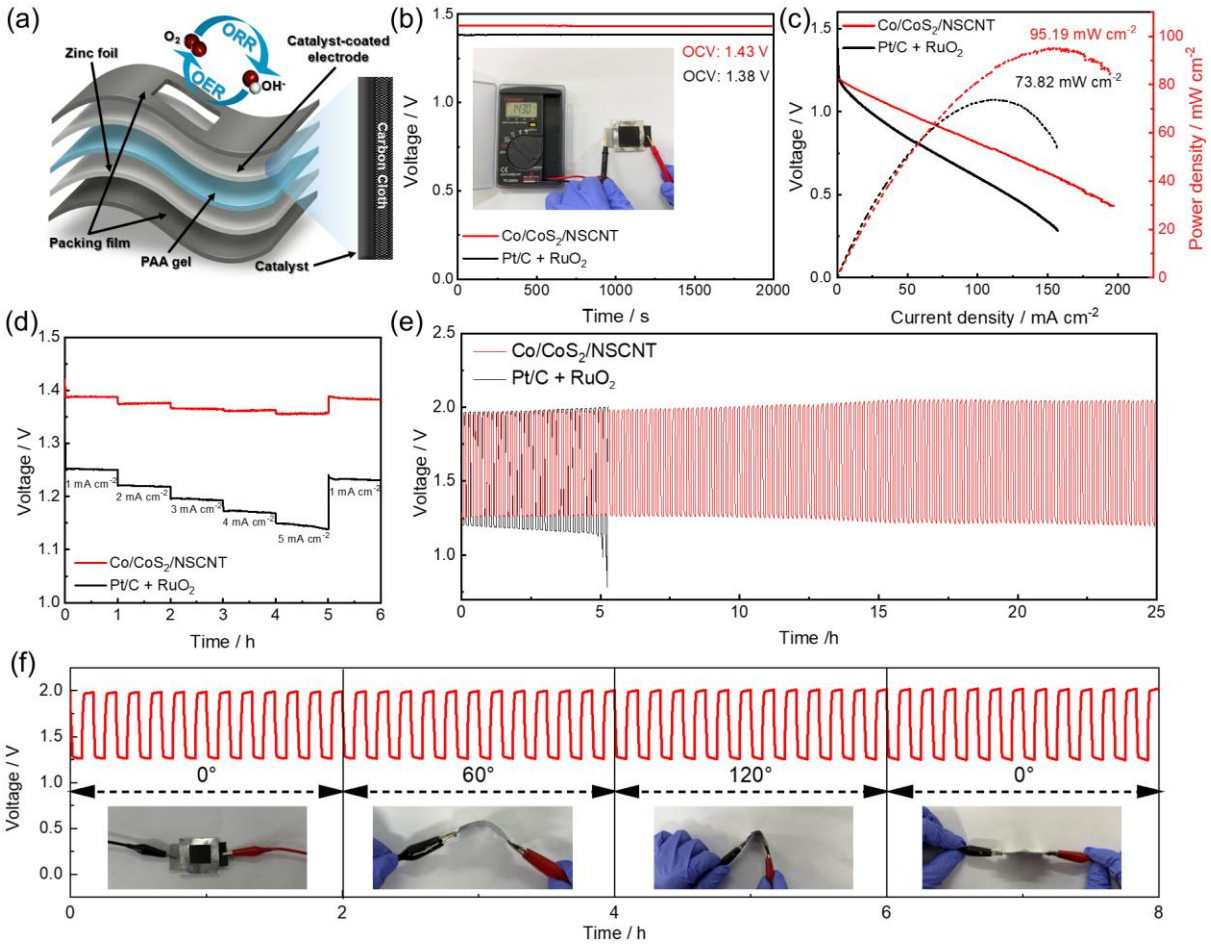


Fig. 7. (a) Schematic illustration of flexible rechargeable ZAB. (b) OCV profiles; the inset shows digital photograph of OCV value for Co/CoS_2/NSCNT-based flexible ZAB. (c) Discharge polarization curves and corresponding power density curves and (d) constant discharge voltage profiles at different current densities. Long-term galvanostatic charge/discharge cycling performance in unbending state (e) and bending state (f).

Supplementary Files

This is a list of supplementary files associated with this preprint. Click to download.

- Supplementarymaterial.docx